Universitetet
i Stavanger

Faculty of Science and Technology
Master's Thesis

Study program/specialization: Marine and Offshore Technology	The (spring) semester, (2024) Open
Author: Mehrzad Falak	
Supervisor: Prof. Muk Chen Ong Co-supervisor: Chern Fong Lee	
Thesis title: Extreme response analysis of a floating offshore wind turbine and Fatigue analysis of the mooring lines	
Credits (ECTS): 30	
Keywords: Wind energy, Floating offshore wind, Mooring system, Synthetic fiber ropes, Intermediate water, Fatigue analysis	Pages: 112 Stavanger, (15.06.2024)

Contents

List of Figures

List of Tables

List of Abbreviations

ABS	American Bureau of Shipping
API	American Petroleum Institute
BEM	Blade Element Momentum
CapEx	Capital Expenditure
DNV GL	Det Norske Veritas and Germanischer Lloyd
DLC	Design Load Case
DOF	Degree of Freedom
EC	Environmental Condition
FOWT	Floating Offshore Wind Turbines
LCOE	Levelized Cost of Energy
MBS	Mean Breaking Strength
MDA	Maximum Dissimilarity Algorithm
MS	Mooring System
NREL	National Renewable Energy Laboratory
PSD	Power Spectral Density
OpEx	Operating Expenses
OWC	Original Working Curve
OWE	Offshore Wind Energy
RAO	Response Amplitude Operator
SN II	Sørlige NordSjø II
TLP	Tension Leg Platform
TDP	Touch down point
WC	Working Curve
WP	Working Point

Acknowledgment

I would like to use this section of the thesis to show my appreciation for the people who helped me in delivering this work. Without their help, this would have been impossible. Firstly, I would like to thank my supervisor, Prof. Muk Chen Ong, for his guidance and continuous feedback and follow-up on the progress. He also helped me grow as an individual by pushing me out of my comfort zone.

Additionally, I would like to thank my supervisor, Chern Fong Lee, who helped me in all steps of this journey with his knowledge and experience. He dedicated so much of his valuable time to helping me learn and implement concepts in this thesis.

Last but not least I would like to thank my family and friends who helped me in my day-to-day life by being there for me and also helping me with keeping a healthy work-life balance.

Abstract

In this study, we evaluate the design of a floating offshore wind turbine mooring system for intermediate water depths of 60 meters. We also analyzed extreme load cases and fatigue analysis of the mooring lines. The mooring system proposed for this case is a 3-segment chain-rope-chain configuration, with polyester rope as the intermediate rope segment. The mooring line's bottom segment and middle segment lengths were modified to reach 10% of the mean breaking strength (MBS) pretension in the polyester segment. The bottom part of the polyester was attached to a buoy to prevent collision with the seabed. To model the nonlinearity of the polyester rope, we used the Syrope method recommended by DNV. This method determines the dynamic stiffness of the mooring line. The environmental conditions at the Sørlige Nordsjø II (SN II) site, located 140 km off the coast of Norway, were analyzed using a joint distribution model from previous studies to determine significant wave height, wave period, and wind speeds.

We proposed five different mooring configurations to be tested and compared. The results suggest that while the mooring system 5 (MS5) configuration provides better platform stability, the MS1 configuration is the preferable design due to its reduction of mooring line maximum loads, standard deviation of the load, and hence fatigue damage. This makes MS1 the best choice among the proposed line configurations for further analysis.

Extreme load cases (DLC16 at 25 m/s wind speed and DLC61 at 43 m/s wind speed) were identified for detailed analysis. The results indicate that DLC61 is more critical for the design than DLC16 due to higher extreme tension and larger platform surge displacement.

To evaluate fatigue, a maximum dissimilarity algorithm (MDA) was first implemented to select representative sea states from a large database of generated sea states. This method resulted

in a manageable number of simulations while trying to represent all of the sea conditions. Fatigue analysis revealed that the chain segment at the fairlead should be the main focus of the fatigue analysis as recommended by API which gives a lower estimated fatigue life. The fatigue life for the chain at the fairlead was estimated to be around 280 years with a safety factor of 1.

In conclusion, this study tries to evaluate the mooring system design for the proposed site off the coast of Norway in 60-meter water depths for wind farm development with a focus on mooring line design and fatigue analysis. This study finds the MS1 to be the best of the five proposed mooring configurations and the extreme response analysis of the mooring line suggests that even at the 50-year return period sea state (DLC61) the extreme mooring line tension reaches around 35% of the MBS. The fatigue analysis also suggests that the chain segment at the fairlead has a suitable estimated life of 280 years (safety factor of 1). These results suggest that MS1 can be a reliable design for the development of a floating offshore wind farm at the proposed site.

1 Introduction

1.1 Background

Offshore wind energy (OWE) is widely recognized as one of the most efficient renewable solutions for reaching carbon net zero and the reduction of the greenhouse effect. The development of offshore wind farms tackles the environmental challenges related to pollution from maritime transportation and the consumption of fossil fuels. Over the past decade, a significant amount of investments in OWE, political support from governments, and advancements in technology, have positioned offshore wind as a big competitor to traditional oil and gas sources. It is estimated that a 55% reduction in the production costs of turbines will happen from 2018 to 2030 [1, 2].

The first offshore wind turbine was installed in Sweden in 1990. In the past two decades, the leading countries in the offshore wind industry are the UK, Germany, Denmark, Sweden, and the Netherlands. Although Norway has great offshore wind resources and the potential to be one of the first producers of clean wind energy it is lagging in these countries. The majority of the wind farms have mainly used bottom fixed platforms for wind turbines such as monopiles and jackets. Since deeper waters with more than 60 meters of depth offer stronger and more consistent winds, traditional bottom-fixed wind turbines become economically infeasible, this makes floating offshore wind turbines (FOWT) a better alternative. The first floating offshore wind turbine was implemented in Italy in 2008 by Blue H Technologies which used a Tension Leg Platform (TLP). A year after this, Equinor installed the Hywind spar platform which was the first FOWT that produced energy above megawatts [3, 4].

Today we have the possibility of installing offshore platforms at far deeper waters thanks to the advent of floating offshore platforms that took inspiration from the platforms in the oil and gas industry including the semisubmersibles, TLPs, etc. [4].

It is expected that offshore wind turbine installations to be accelerated significantly in the near future. For instance, it is projected that Europe will install 129 GW of wind farms between the years 2023 to 2027. One-third of the whole capacity is estimated to be built offshore. However, to meet Europe's green transition goals by 2030, it is required to develop fields with more than 30 GW of power per year. Currently, the evidence suggests that these targets have not been met [5, 6].

FOWTs offer advantages, such as being located far from residential areas which mitigates visual and noise problems for the locals. Additionally, the wind is more consistent and has higher speed as we move further away from the coasts which results in higher efficiency. [4]. One of the most critical factors that influence the development of offshore wind energy, is the levelized cost of energy (LCOE), which needs to be reduced to ensure the profitability of the windfarms [7]. Capital expenditure (CapEx) and operating expenses (OpEx) are two of the main factors that affect the LCOE. Mooring lines play a crucial role in CapEx when designing the FOWTs [8]. Using taut synthetic polyester ropes instead of traditional catenary chain mooring systems is more attractive due to their lower weight and cost-effectiveness. Not only do synthetic ropes exhibit lower overall material costs, but also their installation costs are comparable to those of chain mooring systems [9].

Floating platforms give us the flexibility of turbine installation in deep, intermediate, and also shallow waters. As an example, Zhou et al. used a Novel barge platform in their study to install a turbine in shallow waters [10]. The terms shallow, intermediate, and deep water are based on the

ratio of the water depth to the wave length [11]. The installation of platforms in shallower waters helps with reducing cable and logistical costs as often shallower water is usually closer to the coasts [12]. Although the platforms offer this stability it should be noted that the stiffness of the mooring system is influenced by the water depths at which the platform is located [13, 14].

Figure 1.1 shows traditional catenary mooring lines located in different water depths. As can be seen, the shallower the water the higher the mooring line tension for the same offset. This is due to having more chain lift-off from the seabed with the same amount of offset for the shallow water catenary systems [15, 16]. As the stiffness of the catenary systems is dependent on the mooring hanging weight this means that reducing the water depth for the same platform and subjecting it to the same sea loads results in a faster increase in mooring line tension which can cause higher loads and potentially breaking of the mooring line by reaching MBS. Using synthetic fiber ropes, with nonlinear stiffness and hyper-elasticity, can be a good solution to tackle these challenges in reduced water depths [16].

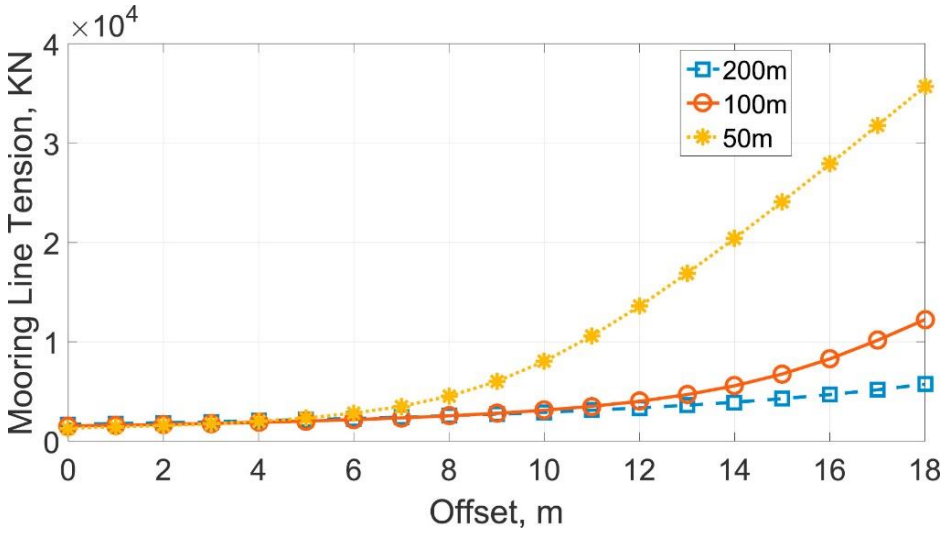

Figure 1.1 Mooring line tension in different water depths vs the horizontal offset of the platform. reproduced from [16].

1.2 Thesis objectives

Norway has immense potential for offshore wind farm development, being bordered by vast sea areas with favorable wind resources. For areas without conflicts, Norway has the potential for 338 GW of offshore wind energy [17]. This study aims to design, analyze, and optimize a floating offshore wind turbine mooring system for one of these areas in intermediate water depths of 60 meters at the Sørlige NordSjø II (SN II). The primary objectives of this research are outlined as follows:

- Design of the mooring system and evaluation of the Platform response and the mooring line's tension
    - Evaluate the environmental conditions at the SN II site using a joint distribution model from previous studies to determine wave height, wave period, and wind speed for numerical analysis.
    - Develop a mooring system for intermediate water depths of 60 meters with a 3-segment chain-rope-chain system.
    - Applying the Syrope method for accurately estimating the mooring line dynamic stiffness for the polyester segment at each sea state.
    - Test five different mooring configurations to identify the most effective design in terms of platform stability, maximum load reduction, and fatigue damage reduction.
    - Selecting the best configuration based on platform and mooring system statistics.
- Predicting the extreme responses
    - Utilizing the Modified Environmental Contour Method (MECM) to predict extreme responses of the mooring system.

    - Identify and analyze critical design load cases (DLC16 and DLC61) to evaluate extreme tension responses and surge displacements.
- Perform fatigue analysis of the mooring line
    - Using the Maximum Dissimilarity Algorithm (MDA) to select representative sea states for fatigue analysis, to reduce the computational cost of simulating many sea states by a few representative sea states while maintaining the quality of estimations.
    - Estimation of the fatigue life of the mooring line following API recommendations.

In summary, this research aims to find a suitable mooring system design for the development of the floating wind turbine at the SN II site off the coast of Norway. To achieve this the sea states at the site are going to be evaluated and then the platform and mooring line will be tested at each of these sea states to find the best mooring configuration. After the selection of the desired mooring system, we implement MECM to evaluate extreme response analysis. We continue with estimating the fatigue damage for the mooring lines. The research goals are to help with the development of the offshore wind turbine in the area of interest by focusing on reducing fatigue damage, ensuring the safety of the mooring lines, and platform stability.

1.3 Thesis outline

This thesis contains five chapters in total. In this section, we will briefly explain what is going to be discussed in each of these chapters except the introduction chapter.

Chapter 2 contains the theoretical background of the thesis. In this chapter, we go over the literature review and the recent trends in offshore wind turbine concepts. We discuss the mooring line theory. We end the chapter by discussing environmental loads on the platform and the wind turbine and structure dynamics.

Chapter 3 discusses the methodology of the thesis. This chapter contains information on the numerical analysis done and their set up. We also discuss the methods and algorithms used in this thesis such as MDA, Rainflow counting etc.

Chapter 4 provides the results and discussion of the thesis. This includes the validation results of the model and outputs of the numerical simulations. In this chapter, we present the global response of the platform and extreme response analysis and at the end of the chapter, we provide the result of the fatigue analysis.

Chapter 5 is the final chapter of the thesis which summarizes all of the findings and provides the conclusion to the thesis.

2 Theoretical Background

2.1 Floating Offshore Wind Turbines

To date, many different concepts have been proposed for Floating Offshore Wind Turbines (FOWTs), with some already implemented while others are still under evaluation and remaining in the conceptual stage. In this section, a brief overview of these proposed concepts is provided. Each concept comes with its advantages and disadvantages when it comes to providing platform stability. Figure 2.1 illustrates the comparison of the methods used by each of these concepts to achieve stability [18].

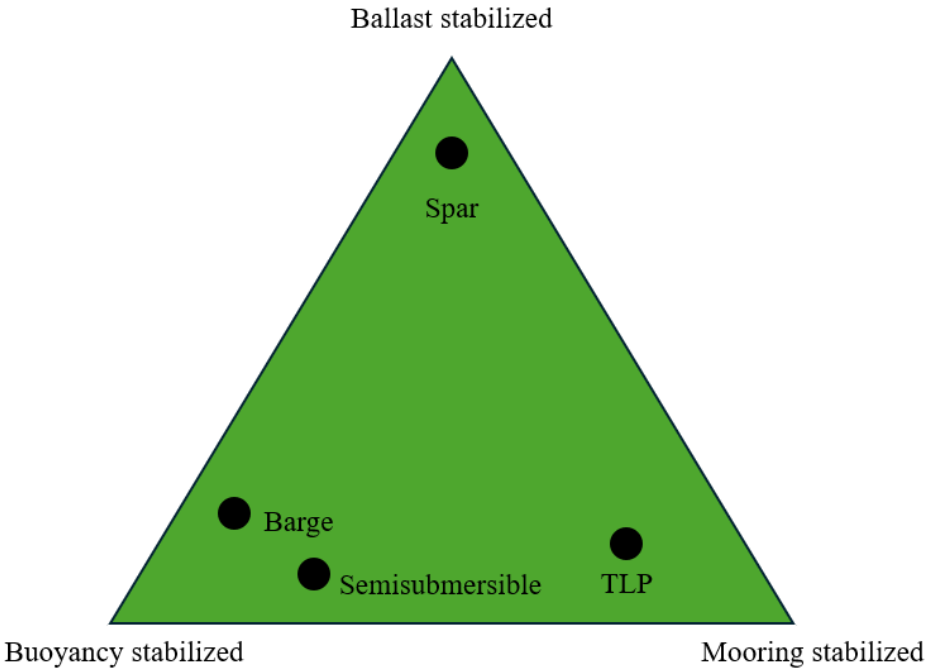

Figure 2.1 FOWT stability triangle adopted from [18].

2.2 Spar Platform

Spars were the first floating wind turbine platform that was used to build the first operational wind farm (Hywind Scotland) by Equinor [3]. These are deep draft cylindrical structures that take advantage of their low center of gravity to achieve excellent hydrodynamic stability. Spars are more suitable for deep waters and have a minimum depth limitation [4, 18].

The simple cylindrical geometry of the Spar platform makes is easy to mass produce. Figure 2.2 shows the Spar platform used by Equinor in the first operational floating offshore wind farm. As can be seen in the figure mooring lines were used to provide the restoring stiffness to the Spar platform. The platform itself is primarily stabilized through ballasting.

2.2.1 Semisubmersible Platform

These structures usually consist of columns attached to pontoons. Due to their low draft, they can easily be manufactured onshore or at ports and then towed to their position. This makes their manufacturing and installation rather simpler and inexpensive compared to other platforms [4].

Figure 2.3 shows different semisubmersible platform concepts used for FOWT. At the time of writing this thesis Kincardine Offshore Wind is the largest semisubmersible project (in terms of power rating) that uses the WindFloat platform developed by Principal Power to operate in Portugal with a capacity of 8.4 MW [19]. The WindFloat concept has the advantage of wind turbines being installed on the side of the platform (instead of the center) which makes operation and maintenance easier due to easier vessel accessibility [4, 18].

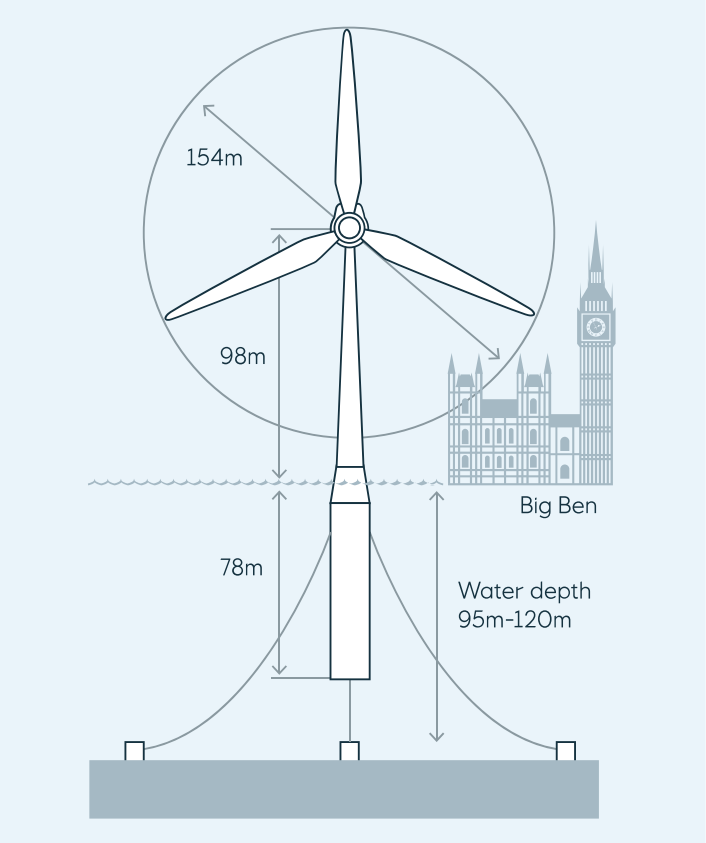

Figure 2.2 The Spar platform used by Equinor in the first operational floating offshore wind farm reproduced from [20].

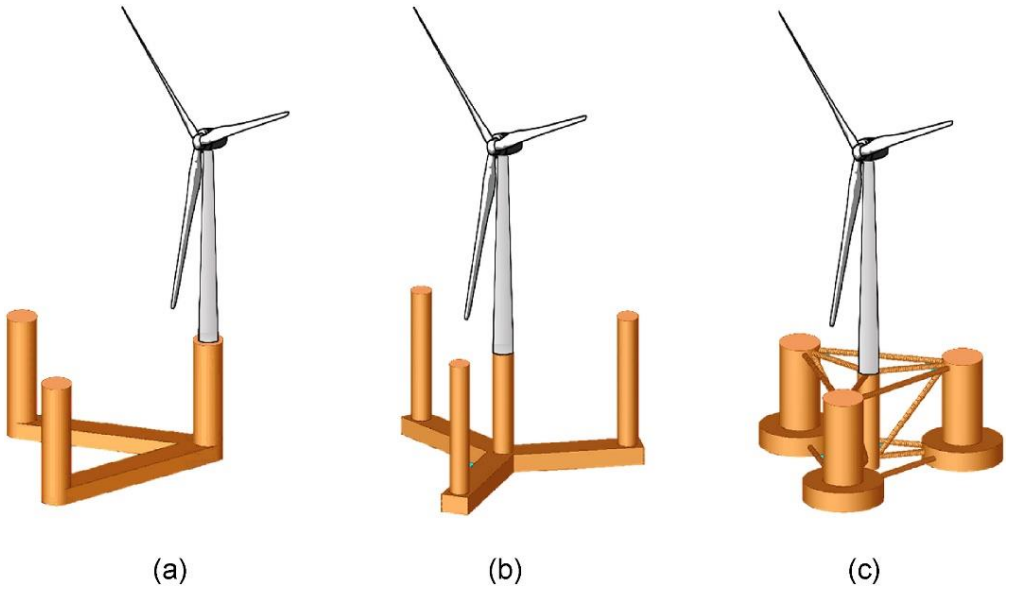

Figure 2.3 Several different semisubmersible platforms for offshore wind reproduced [21].

2.2.2 Barge Platform

Barge platforms have the advantage of large waterplane areas which gives them high hydrodynamic stability like the semisubmersibles and, they have the potential for mass production due to their simple geometry like Spar platforms [4, 18]. The Floatgen concept made by BW Ideol is an example of this type of platform that also contains a moonpool in the center (Figure 2.4) that reduces the floater motion by the absorption of wave loads [22]. This absorption of energy is known as the moonpool damping effect which causes a reduction of the dynamic response of the platform to horizontal and rotational motions [23, 24].

Figure 2.4 Floatgen concept made by BW-Ideol reproduced from [25].

2.2.3 Tension Leg Platforms

These platforms use their high buoyancy to put tension on the vertical tendons attaching them to the seabed [26]. These platforms are suitable for deeper waters due to their excellent stability in water depths of 500m and above where extreme waves can occur [27]. As these platforms rely heavily on the tendon's pretension, a failure in the tendons would have the risk of capsizing the platform [28].

2.2.4 Other concepts

In recent years many different platform concepts have been proposed. Many of these are based on existing designs or are inspired by other technologies used in the making of yachts and other offshore vessels. Figure 2.5 shows one of these concepts based on the design of a catamaran which is known to have excellent stability based on previous experience within the transportation and recreational industries [18]. Additionally, other concepts have been proposed with the combination of existing technologies. For example, increasing the draft of the platform combines the advantages of both semisubmersible and spar platforms into one design by lowering the center of gravity. Another concept is increasing the water plane area by inclining the vertical columns of the semisubmersibles. This concept can be seen in Figure 2.6 [29].

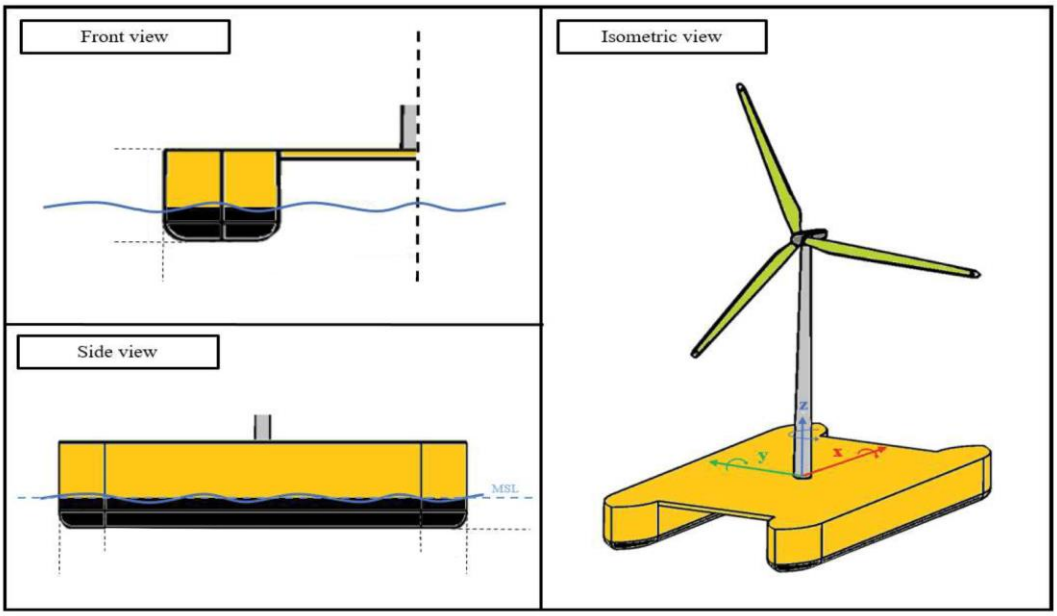

Figure 2.5 Catamaran floating platform concept reproduced from [18].

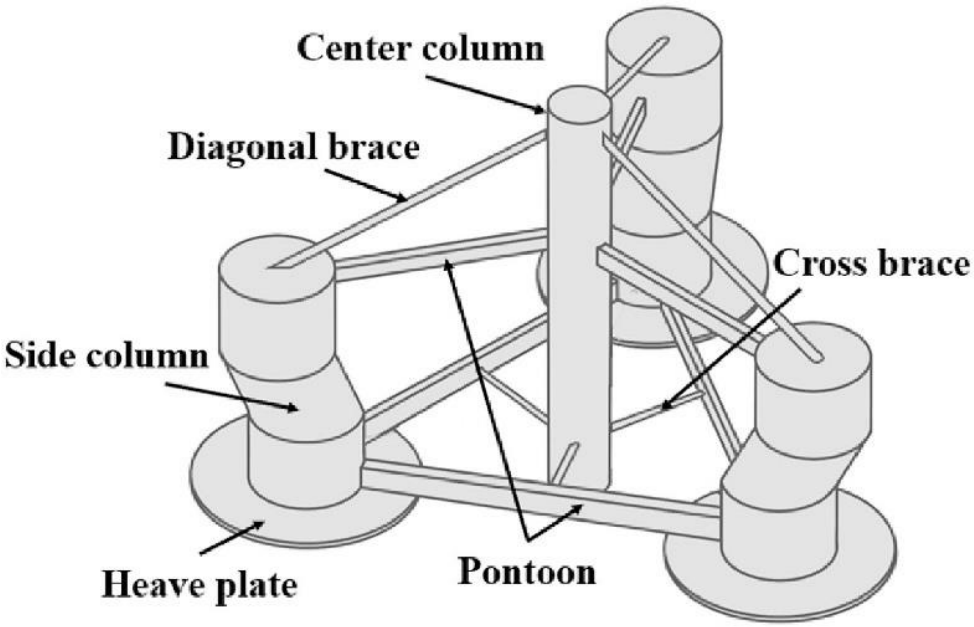

Figure 2.6 Fully Submerged platform concept reproduced from [29].

2.3 Mooring System

The mooring system's main purpose is to limit the horizontal movement of the floating platform. The most common type of mooring system in the industry has been catenary for floating offshore structures. These mooring systems provide the restoring force through the hanging mass of the mooring system. When considering the windward mooring line (the mooring line located on the side the wind is blowing from), the horizontal offset of the floating platform causes the mooring line at the seabed to lift be lifted from the seabed. This adds more hanging mass to the mooring system which increases the restoring force of the system. Figure 2.7 shows such catenary systems' static configuration in 200-meter water depth which is used for validation of this studies.

The stiffness of mooring lines comprises two components: elastic and geometric stiffnesses, as mentioned by Faltinsen [30]. The combined stiffness and each of these stiffness components can be determined using the following equations:

$$\frac{1}{K} = \frac{1}{K_g} + \frac{1}{K_e} \qquad \text{(Equation 2.1)}$$

$$K_g = w\left[\frac{-2}{\left(1+\frac{2T_H}{wh}\right)} + \cosh^{-1}\left(1+\frac{wh}{T_H}\right)\right]^{-1} \qquad \text{(Equation 2.2)}$$

$$K_e = \frac{EA}{l}\cos\alpha \qquad \text{(Equation 2.3)}$$

where l represents the total length of the mooring line, w represents the mooring line weight per length, α represents the angle between the line and the seabed and T corresponds to the tension in the mooring line, with T_H represents its horizontal component.

The effective weight of the mooring line is the submerged weight of the hanging weight of the line which contributes to the restoring stiffness of the whole mooring system [31]. By relocating to shallower waters, the effective weight of the mooring system decreases since the length of the hanging portion of the chain is reduced. This results in reduced restoring stiffness of the catenary mooring lines. To alleviate this problem, it is required to increase the anchor radius. Zheng et al. [32] conducted a comparative analysis between catenary and tensioned mooring systems (mooring systems that are pre-tensioned before installation) in shallow waters. It was found that the tensioned mooring systems result in more stable platforms. This was concluded due to lower mean platform surge offset observation for tensioned mooring systems compared to those of the traditional catenary systems. However, it is worth noting that this resulted in a slightly higher standard deviation in platform surge motion. Other parameters such as average heave, pitch of the platform and mooring line tension values remain similar between the two designs, although the mooring line tension standard deviation was found to be notably higher for the tensioned mooring systems.

In addition, Lozon et al. [33] demonstrated that polymer ropes have the advantage of reducing peak loads during extreme environmental conditions (extreme sea state at wind turbine operational state and 50-year return period sea state in the parked state). Although this was at the cost of more surge offset of the platform the displacements were found to be below the allowed displacement limit. Additionally, the reduction of peak mooring tension was found to be even more effective at the extreme 50-year sea state than at the extreme state at the rated wind. This behavior was attributed to polymeric rope's high elasticity and stretch capacity under extreme loads. According to this study, the use of polyester ropes can be beneficial in reducing peak loads by up to 60% in a 50-year sea state, which is advantageous in reducing fatigue damage in polyester ropes.

2.4 Environmental loads on the floating offshore wind turbines

Floating offshore wind turbines are mainly subjected to aerodynamic loads from winds, and hydrodynamic loads from waves and currents. The combination of these loads contributes to the motions of the platform and the structural dynamics. In this section, we will briefly discuss the aerodynamic and hydrodynamic loads and continue with the structural dynamics according to the documentation provided by SINTEF [34].

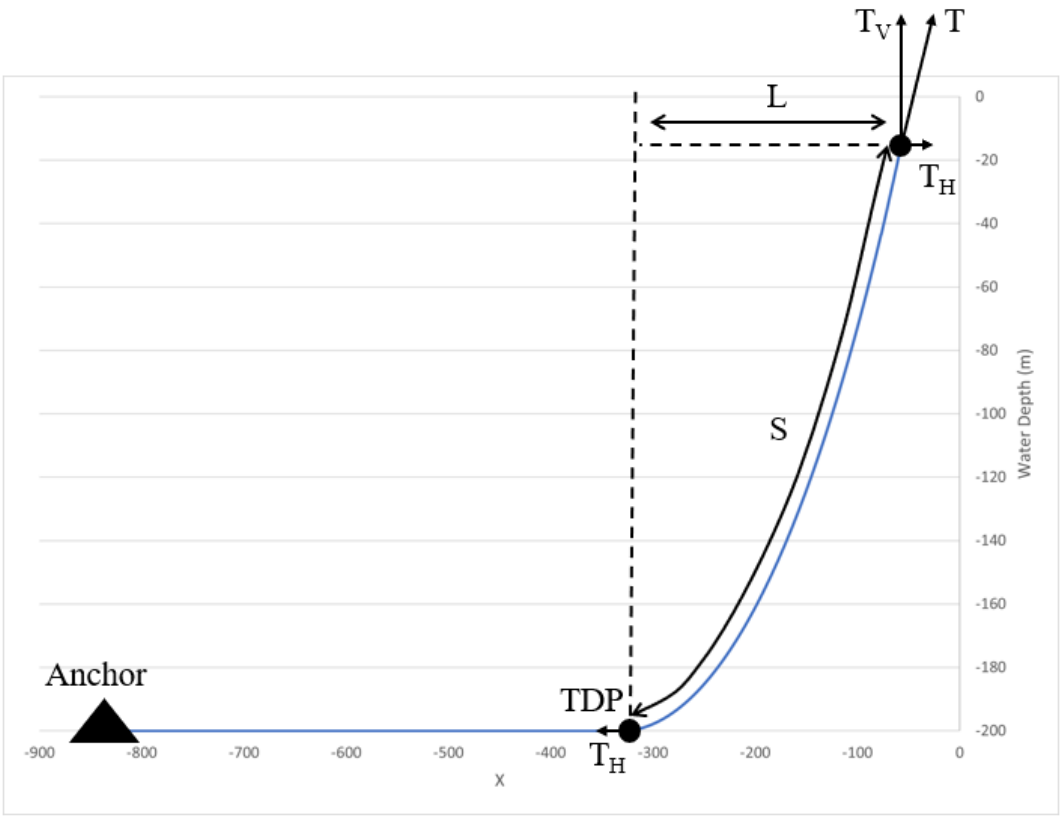

Figure 2.7 Catenary mooring line static configuration at 200-meter water depth. S represents the hanging chain length, and L is the horizontal distance between the fairlead and touch-down point (TDP).

2.4.1 Aerodynamic loads

Aerodynamic forces play an important role in the operations of FOWT. These forces include drag, lift, and blade moment loads. These loads can be applied to the airfoils or other elements that are exposed to wind. To calculate these forces the equations below can be used:

$$F = C_{Dx}U^2 + C_{Dy}V^2 + C_{Dz}W^2 \quad \text{(Equation 2.4)}$$

$$C_{Di} = \frac{1}{2}\rho_{air}S_{2D}C_{di} \quad \text{(Equation 2.5)}$$

In which U, V, and W are the relative speed of the component in x, y, and z directions. C_{Di} is the aerodynamic drag coefficient in the i direction. S_{2D} is the cross-sectional area of the element and C_{di} is the non-dimensional aerodynamic coefficient. With the help of these coefficients which can be found in standard tables, we can determine the drag, lift, and moment forces with their corresponding coefficients C_D, C_L and C_M as follows:

$$F_D = \frac{1}{2}C_D\rho_{air}c(V_x^2 + V_y^2) \quad \text{(Equation 2.6)}$$

$$F_L = \frac{1}{2}C_L\rho_{air}c(V_x^2 + V_y^2) \quad \text{(Equation 2.7)}$$

$$F_M = \frac{1}{2}C_M\rho_{air}c^2(V_x^2 + V_y^2) \quad \text{(Equation 2.8)}$$

Additionally, to account for the aerodynamic loads acting on airfoil the blade element momentum (BEM) theory is applied. This is the method that is applied in SIMA/RIFLEX for the

aerodynamic load calculations and the principle behind this is the balance of momentum change for the air that is flowing through the rotor disk area with the empirical drag and lift coefficient.

2.4.2 Hydrodynamic loads

In SIMO/RIFLEX the hydrodynamic loads that are accounted for consist of first-order and second-order wave loads on the structure and also Morison equation is also used for current forces on the mooring lines and slender structures.

The first-order wave loads are the result of the direct and linear interaction of the waves on the structure such as the heave motion of the platform as soon as it comes into contact with a wave. The first-order wave loads are usually the largest hydrodynamic forces exerted on the platforms. First-order wave loads consist of Froude-Krylov, diffraction, and radiation forces. These forces can be calculated by solving the potential flow theory with appropriate boundary conditions [35].

The Froude-Krylov force can be measured by knowing the pressure field around the structure by solving the integral of the pressure field around the structure using the equations below:

$$P\ (x,z,t) = \rho g \eta(x,t) \frac{\cosh(k(z+h))}{\cosh(kh)} \quad \text{(Equation 2.9)}$$

$$F_{FK} = \int_s P(x,z,t) n ds \quad \text{(Equation 2.10)}$$

Where η is the wave elevation, k is the wave number, z is the vertical distance from sea level, h is the water depth and n is the normal vector direction from the structure surface.

The second-order waves are the result of the wave's interaction with each other and the platform. These loads are generally not as strong as the first order but they are important to consider since they can cause resonance and fatigue damage. These are solved by the second-order diffraction potential theory. These forces can be divided into two types including the sum-frequency loads and difference-frequency loads [36, 37].

$$F_{sum}\,(t) = \sum_{i,j} Q_{sum}\,(\omega_i, \omega_j) A_i A_j e^{i\,(\omega_i+\omega_j)t} \qquad \text{(Equation 2.11)}$$

$$F_{diff}\,(t) = \sum_{i,j} Q_{diff}\,(\omega_i, \omega_j) A_i A_j^{*} e^{i\,(\omega_i-\omega_j)t} \qquad \text{(Equation 2.12)}$$

Where Q is the quadratic transfer function, ω is the wave frequency and A is the wave amplitude with A^* being the complex conjugate of the wave amplitudes.

Lastly, the Morison equation can be used for measuring the loads on slender structures which are structures such as mooring lines with small diameters compared to the wavelength. The Morison equation is given as:

$$F\,(t) = \frac{1}{2}\rho C_d D|U|U + \rho C_m V \frac{dU}{dt} \qquad \text{(Equation 2.13)}$$

Where C_d is the drag coefficient, ρ is the fluid density, D is the slender structure diameter, U is the flow velocity, and V is the displaced volume per unit length.

2.5 Structural dynamics

The structural dynamics of the FOWT can be analyzed by solving the time domain fully coupled equation of motion. The general form of this equation is:

$$F\ (x, t) = M\ x + C\ \dot{x} + K\ \ddot{x} \qquad \text{(Equation 2.14)}$$

Where M is the mass matrix, C is the damping matric, K is the stiffness matrix and these can be determined according to the platform geometry and configuration. F represents the total forces on the structure and can be determined from what was explained earlier to solve for the displacement of the structure [38].

3 Methodology

3.1 Problem description

3.1.1 The platform, wind turbine, and mooring system

In this study, the Sørlige NordSjø II site, which is situated approximately 140 kilometers off the coast of Norway, was selected as the site of interest for the wind turbine. With a water depth of 60 meters at the site, a semi-submersible platform with a low draft of 20 meters and 4 columns with the central column accommodating the turbine was selected as the most suitable concept to accommodate a 15MW wind turbine. Figure 3.1 represents a schematic for the FOWT concept. For station keeping, a semi-taut mooring system was designed, which consists of a chain-rope-chain configuration. The same model with a pure chain catenary system in 200 meters depth was used to validate the results against that of the University of Maine in 200 meters water depth reported by NREL [39]. A buoy was attached to the bottom end of the polyester rope to ensure this section does not have any contact with the seabed. A schematic representation of this system is shown in Figure 3.2. In the study, the length of the top chain segment remains constant (50 meters). The top chain's main purpose is to prevent abrasion. Abrasion happens when polyester is in direct contact with the fairlead.

The floating offshore wind turbine (FOWT) utilized in this study comprised the University of Maine VolturnUS-S steel semisubmersible platform and the International Energy Agency (IEA) 15MW reference wind turbine. Table 3.1 provides a detailed description of the reference turbine and platform properties.

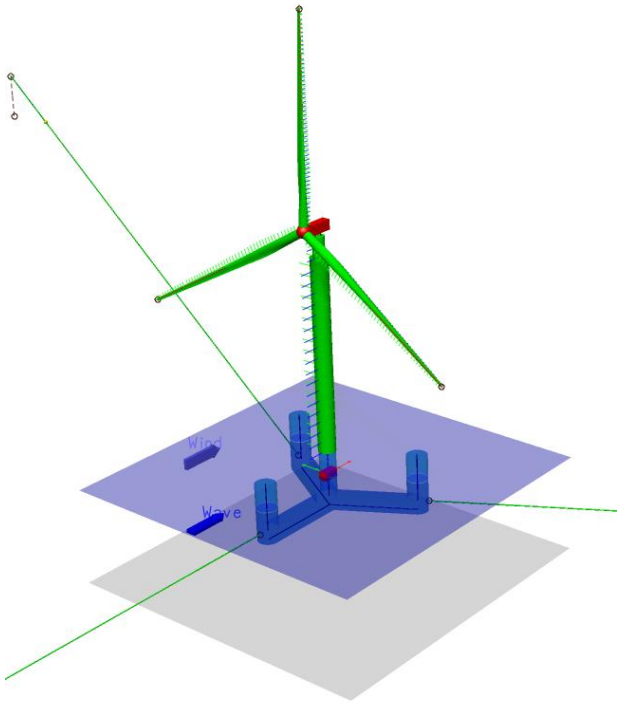

Figure 3.1 VolturnUS-S platform with the IEA 15MW wind turbine.

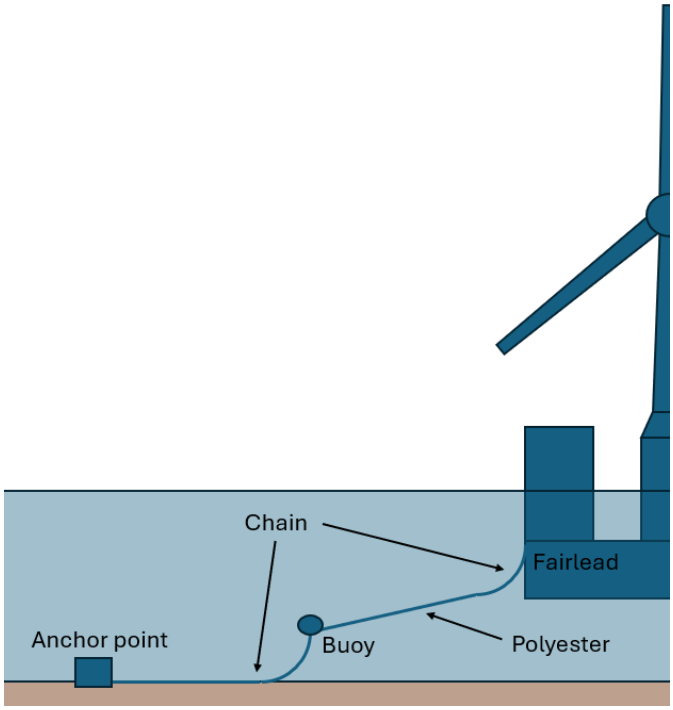

Figure 3.2 Floating platform mooring configuration.

Table 3.1 Properties of the reference VolturnUS-S FOWT.

Property	Value
Platform	
Water depth (m)	200
Draft (m)	20
Freeboard (m)	15
COG vertical from SWL (m)	-14.94
COB vertical from SWL (m)	-13.63
Roll inertia about COG (kg m^2)	1.25110^{10}
Pitch inertia about COG (kg m^2)	1.25110^{10}
Yaw inertia about COG (kg m^2)	2.36710^{10}
Hull displacement (m^3)	20206
Hull steel mass (tonne)	3914
Ballast mass (tonne)	13840
Buoyancy volume (m^3)	30
Mooring system	Three catenary chains
Wind turbine	
Rating (MW)	15
Hub height (m)	150
Tower mass (tonne)	1263
Roter and nacelle mass (tonne)	991
Tower interface mass (tonne)	100

3.1.2 Semi-taut mooring system

To adapt the mooring system for an intermediate water depth of 60 meters, we replaced the pure catenary system of the reference wind turbine with a 3-segment chain-rope-chain system. The top chain segment was kept at a constant length of 50 meters, while the anchor radius remained fixed. The lengths of the intermediate polyester rope and the bottom chain were adjusted to achieve

a specific pretension value in all designs, set at 10% of the Minimum Breaking Strength (MBS). The buoyancy volume was set to 30 m^3 for all cases.

The material properties of the polyester rope were based on specifications from BRIDON BEKARET [40], and the catenary chain was selected to have a similar MBS to that of the polyester rope. Consequently, the ORQ stud chain was chosen according to specifications from Ramnäs [41]. Additionally, a subsea buoy was attached to the bottom section of the polyester rope to prevent it from touching the seabed.

Table 3.2 shows the properties of the mooring lines used in this study. Notice that axial stiffness for the polyester rope is based on the syrope model that is going to be explained in section 3.4.

Table 3.2 Mooring line properties.

	Nominal diameter (m)	MBS (kN)	Linear density (kg/m)	Axial stiffness (kN)
Chain	0.130	11932	370	1706900
Polyester	0.203	11772	26.5	Syrope Method

3.2 Numerical analysis

To conduct a fully coupled time-domain analysis of the VolturnUS-S platform and its mooring system, we utilized SIMA software, developed by SINTEF Ocean. Tailored for marine applications, SIMA is a dynamic simulation workbench renowned for its comprehensive capabilities in analyzing marine operations and floating systems [42].

3.3 Floating Offshore Wind Turbine

The floater and hub were represented as rigid bodies with concentrated mass in our model. For the submerged parts of the model, WADAM, a hydrodynamic analysis package developed by DNV for assessing wave-structure interactions [43], was utilized to measure hydrodynamic added mass, potential damping coefficients, and first-order wave excitation loads in the frequency domain.

Moreover, the blades, tower, and mooring lines were represented as distributed mass elements, with the mooring lines modeled as bar elements and the blades and tower as beam elements. Buoys were depicted as points with concentrated mass and defined volume. The generator was simulated as two distinct components: a rotating part and a stationary part, connected by a flexible joint.

The fully coupled time domain analysis was conducted using SIMA which solves the structural dynamic equation in the time domain by solving:

$$R^I(r,\ddot{r},t) + R^D(r,\dot{r},t) + R^S(r,t) = R^E(r,\dot{r},t) \qquad \text{(Equation 3.1)}$$

Where R^I is the inertia force vector, R^D the damping force vector, R^S is the inertial structural reaction force vector, and R^E is the external force vector. t is the time and $r, \dot{r}, \ddot{r}$ represent the displacement, velocity, and acceleration respectively.

3.4 The Syrope Model

Synthetic ropes show a non-linear relation between the axial stiffness and their stretch. Due to this behavior modeling these types of mooring lines are not as straightforward as the traditional catenary chain with constant stiffness and new methods for replicating their behavior were proposed. One of these methods is the syrope model that was developed by Falkenberg et al. [44] and is currently the recommended approach to modeling non-linear mooring ropes by DNV [45]. The syrope method has been validated for synthetic mooring lines and provides an accurate approach for modeling polyester ropes.

The syrope method can be represented by a spring dashpot model as represented in Figure 3.3. As shown in the figure the rope can be modeled by two different stretch types. One is the permanent stretch and the other part is the elastic stretch. The permanent stretch in the syrope model is assumed to be accounted for by pretension. The mooring line needs to be tensioned to the maximum expected tension during the installation process. By doing only the elastic stretch section of the mooring dashpot needs to be considered [46, 47]. To further simplify the model, we need to find a solution to remove the visco-elastic section (slow spring) of the model. To achieve this we can account for the elongation of the rope from the visco-elastic stretch then the model can only be represented by the instant elastic stretch (fast spring).

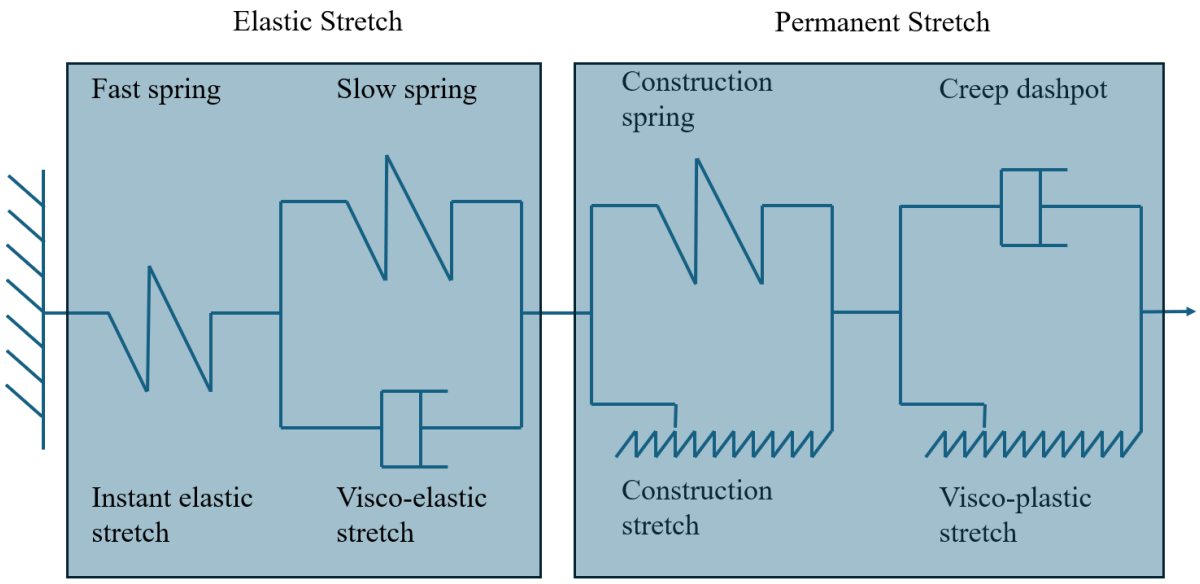

Figure 3.3 Spring dashpot model for the synthetic fiber ropes developed by Falkenberg et al. Adopted from [44].

Figure 3.4 shows the nonlinear behavior of the fiber ropes that was explained earlier. The figure consists of several curves which describe this behavior. These curves consist of the original working curve (OWC), working curve (WC), and dynamic curve. The OWC (green line) is derived from the slow loading of the synthetic mooring line. This is the curve that the mooring line follows during its preinstallation to its maximum tension ($\bar{T}_{max}$). If the mooring line goes beyond this maximum tension during the operation then it follows the same OWC again and results in more permanent stretch. When the load is removed or goes below the $\bar{T}_{max}$, the stiffness of the mooring line increases and follows the WC (blue line). The working curve slope is the static stiffness of the mooring line. The working point (WP) is the point on the blue line at the mean tension ($\bar{T}$). The WP is represents the strain and mean tension around which the dynamic low-frequency and wave-frequency loads occur. The dynamic stiffness curve (brown curve), can be evaluated as a linear curve that passes the WP. These curves can be derived from experimental testing [48].

In this study, we used the simplified method for measuring the stiffnesses according to the previous study by Fjermedal et al. [13]. The static stiffness (EA_s) and the dynamic stiffness (EA_d), of the rope (slopes of the blue and brown curves respectively) needs to be determined for each environmental condition with varying mean tension ($\bar{T}$). The following equations were utilized to calculate the values of both stiffnesses:

$$EA_s = a\bar{T} + bMBL \quad \text{(Equation 3.2)}$$

$$EA_d = c\bar{T} + dMBL \quad \text{(Equation 3.3)}$$

Here, MBL denotes the mean breaking load, while a, b, c, and d represent constants derived from experimental data, sourced from prior studies. the values for these parameters are presented in Table 3.3 [13].

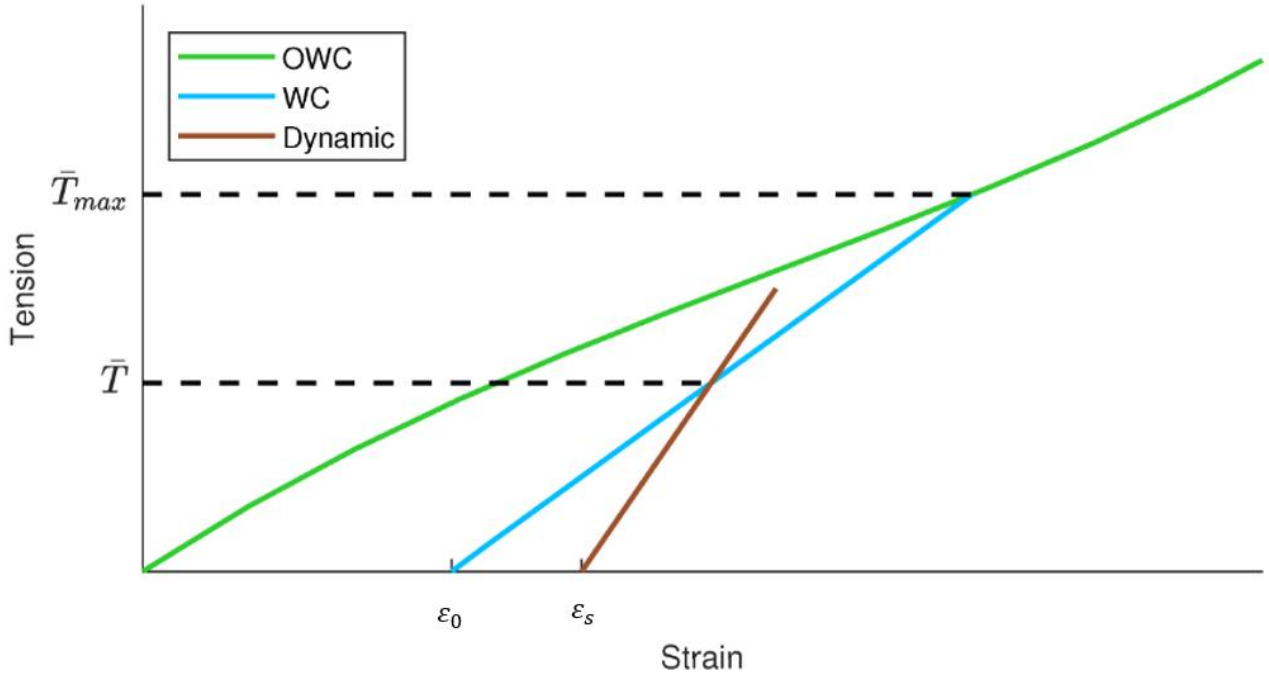

Figure 3.4 The Syrope model illustration reproduced from [48].

Table 3.3 Syrope equation parameters for dynamic and static stiffness.

Parameter	a	b	c	d
Value	50	5.5	25	20

As mentioned, before we need to adjust the rope length after measuring the dynamic stiffness. The new rope length can be measured by finding the stress-free strain of the rope by using Equation 3.4:

$$\varepsilon_0 = \varepsilon_s - \frac{\bar{T}}{EA_d} \quad \text{(Equation 3.4)}$$

Here, ε_0 represents the stress-free strain resulting from permanent deformation, while ε_s is the stress obtained from the static simulation using the static stiffness.

The following procedure shows the steps used to implement the simplified syrope method and the flowchart of the process is presented in Figure 3.5.

1. Initially, we made an educated guess for the initial stiffness (EA_s) of the mooring lines in each environmental condition (EC).
2. The mean tension ($\bar{T}$) obtained from each simulation was then extracted and utilized in the static stiffness equation to calculate an updated value for the stiffness (EA_s). This iterative process continued until the value of static stiffness converged.
3. Subsequently, the converged mean tension was employed to estimate the dynamic stiffness (EA_d).

4. Before running the dynamic simulations, it was necessary to measure the new stress-free rope length. To validate the accuracy of the derived values, comparisons were made between the mean tensions and platform surge displacement obtained from the static and dynamic simulations, as they were expected to yield similar results.

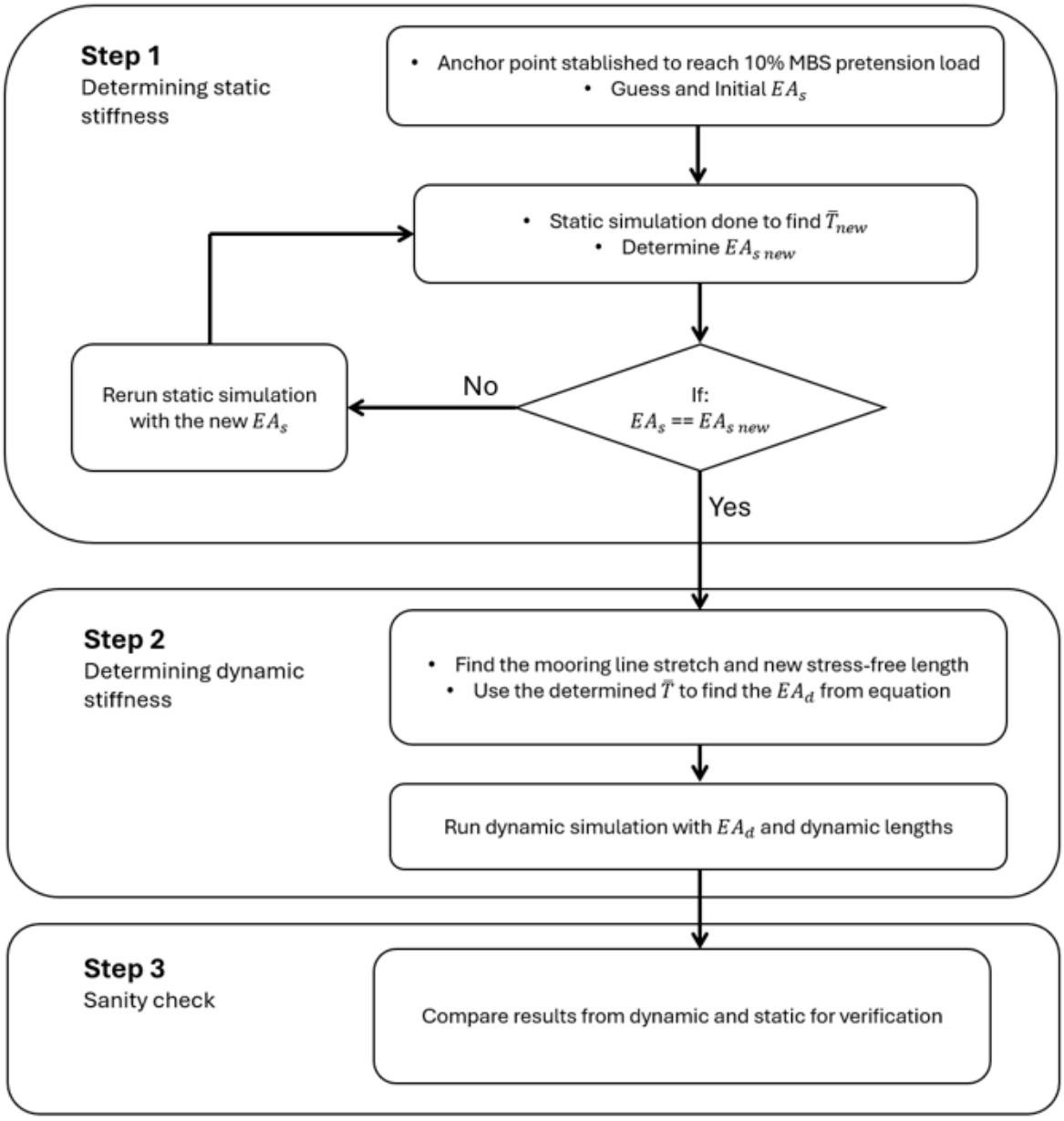

Figure 3.5 Simulation procedure for determining the polyester mooring line static and dynamic stiffness and new stress-free lengths. Adopted from [13].

3.5 Environmental conditions and design load cases

In 2022, the Norwegian government designated the SN II site for offshore wind farm development. Located 140 km off the coast of Norway, this area features water depths ranging from 50 to 70 meters. The joint distribution for this area was fitted as part of the IEA Task 49 WP1, aimed at the continued development of reference wind arrays [49].

In this study, to select the extreme load cases, the model was subjected to various environmental conditions with wind speeds ranging from 10 m/s to 43 m/s, which correspond to just below rated wind speed and the 50-year extreme wind speed, respectively. For each wind speed in this range, the corresponding most probable wave period and wave height were selected. Table 3.4 provides all the environmental conditions (ECs) that were analyzed in this study. The current speed profiles used for the DLCs are also provided in Table 3.5. It is worth mentioning that the software TurbSim was used in this study to generate six different seeds for each EC in this study. The most probable 3-hour extreme tension on the windward mooring line was fitted to a Gumbel distribution using six different seeds for each sea state (Figure 3.6).

Table 3.4 Environmental conditions used for assessment of the platform response and design load cases.

EC	U_W (m/s)	TI (%)	H_S (m)	T_p (s)	Current
01	4	3.76	0.87	5.49	-
02	6	3.99	0.98	5.68	-
03	8	4.22	1.13	5.93	-
04	10	4.45	1.34	6.26	-
05	12	4.68	1.63	6.68	-
06	14	4.91	2.03	7.22	-
07	16	5.14	2.58	7.89	-
08	18	5.37	3.27	8.64	-
09	20	5.60	4.00	9.36	-
10	22	5.83	4.75	10.04	-
11	24	6.05	5.41	10.61	-
12	26	6.17	5.75	10.88	-
13	28	6.28	6.08	11.15	-
14	30	6.51	6.75	11.66	-
15	32	6.74	7.41	12.15	-
16	34	6.97	8.08	12.63	-
17	36	7.20	8.74	13.09	-
18	38	7.43	9.41	13.55	-
19	40	7.66	10.08	13.99	-
20	42	7.89	11.44	14.43	-
21	43	8.21	11.78	14.86	-
DLC 1-6	10.59	4.52	8.07	12.68	1-year return period
DLC 6-1	43.00	8.23	12.54	15.59	5-year return period

Table 3.5 Current profiles used for design load cases.

Depth [m]	Current speed [m/s] at return period [years]					
	1	5	10	50	100	500
0	0.82	0.98	1.05	1.21	1.27	1.42
3	0.76	0.92	0.99	1.15	1.22	1.38
10	0.69	0.85	0.92	1.09	1.17	1.36
15	0.66	0.81	0.88	1.06	1.14	1.35
25	0.58	0.72	0.79	0.98	1.07	1.32
50	0.45	0.58	0.65	0.83	0.92	1.17
55	0.42	0.54	0.61	0.78	0.86	1.09
57	0.40	0.52	0.58	0.74	0.82	1.04
59	0.35	0.46	0.52	0.66	0.73	0.93
60	0.00	0.00	0.00	0.00	0.00	0.00

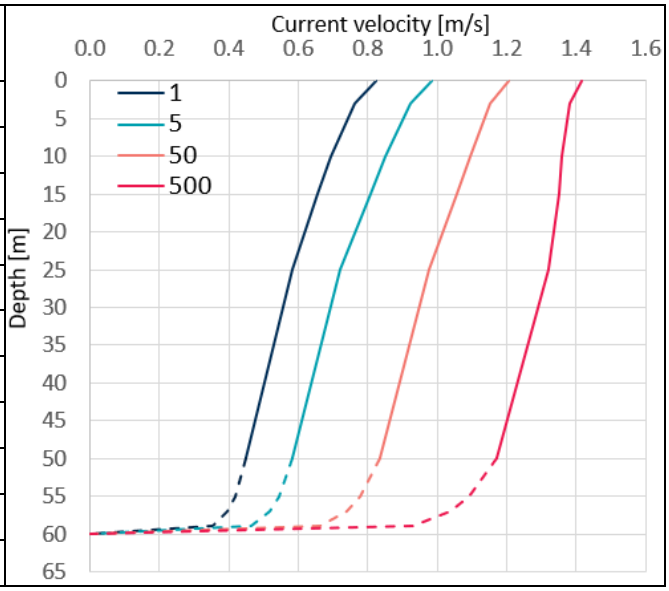

As illustrated in Figure 3.6, the most probable extreme tension increases with wind speed until a sudden drop at the cut-out wind speed due to the control system. After the cut-out wind speed, the extreme tension is primarily due to the wave motions of the platform and is not directly influenced by the wind. Based on the results of these simulations, the design load cases (DLCs) chosen for the extreme load case analysis are at wind speeds of 25 m/s and 43 m/s, with the first being the cut-out wind speed and the second being the 50-year extreme wind speed. It should be noted that the 25 m/s wind speed sea state was extrapolated to have the same 50-year return period as well.

These two states correspond to DLC 1.6 and DLC 6.1 in accordance with IEC 61400-3-1. For DLC 1.6, the sea state consists of the 50-year extreme sea state at cut-out wind speed and the 1-year extreme current speed. In contrast, DLC 6.1 involves the 50-year extreme wind speed and the corresponding 50-year sea state with the 5-year extreme current speed.

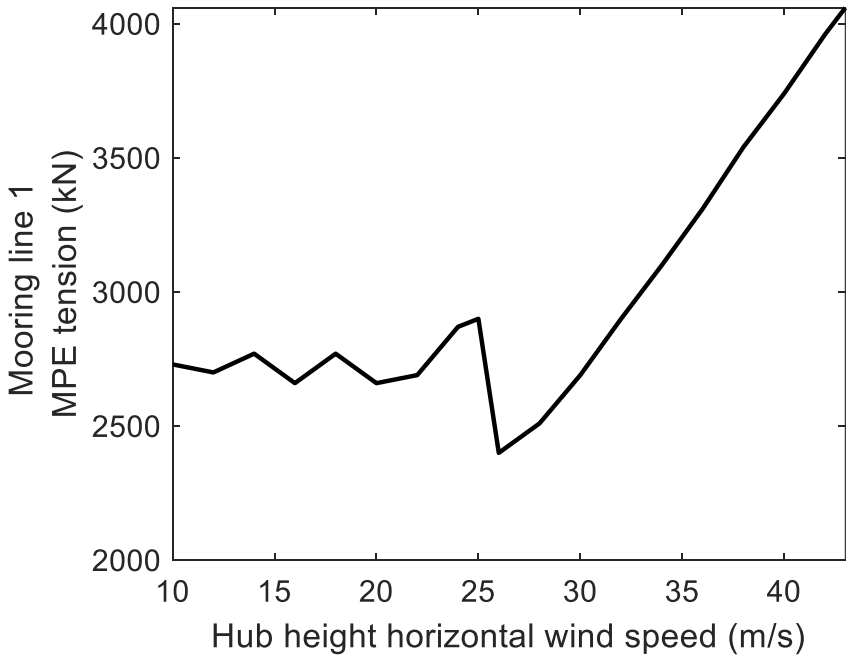

Figure 3.6 The windward mooring line most probable 3-hour extreme tension vs hub height wind speed.

3.6 Validation

To validate the numerical analysis results, we measured the response amplitude operator and natural periods of the floating platform at a water depth of 200 meters. We then compared these measurements against those of the reference VolturnUS-S wind turbine as reported by NREL [39].

To determine the natural periods of the platform, we conducted decay tests. During these tests, the platform was placed in a parked state with blades feathered to minimize the aerodynamic loads, and no external forces such as wind, waves, or currents were applied (i.e., no sea state). A constant load or moment was applied in each of the three Eulerian directions. After a set period, the load was removed, and the platform was left to decay over time. The time intervals between

peak responses and after the load removal were measured as the natural periods in their respective degrees of freedom. Figure 3.7 illustrates the decay tests conducted for surge and yaw, respectively.

To assess the Response Amplitude Operator (RAO), the platform was exposed to regular waves of 1-meter height (2m amplitude) with varying wave periods from 2.5 to 30 seconds, spaced at 2.5-second intervals. The obtained results were then compared against those documented in the NREL report. Each simulation lasted for 5000 seconds, consistent with the duration in the NREL report.

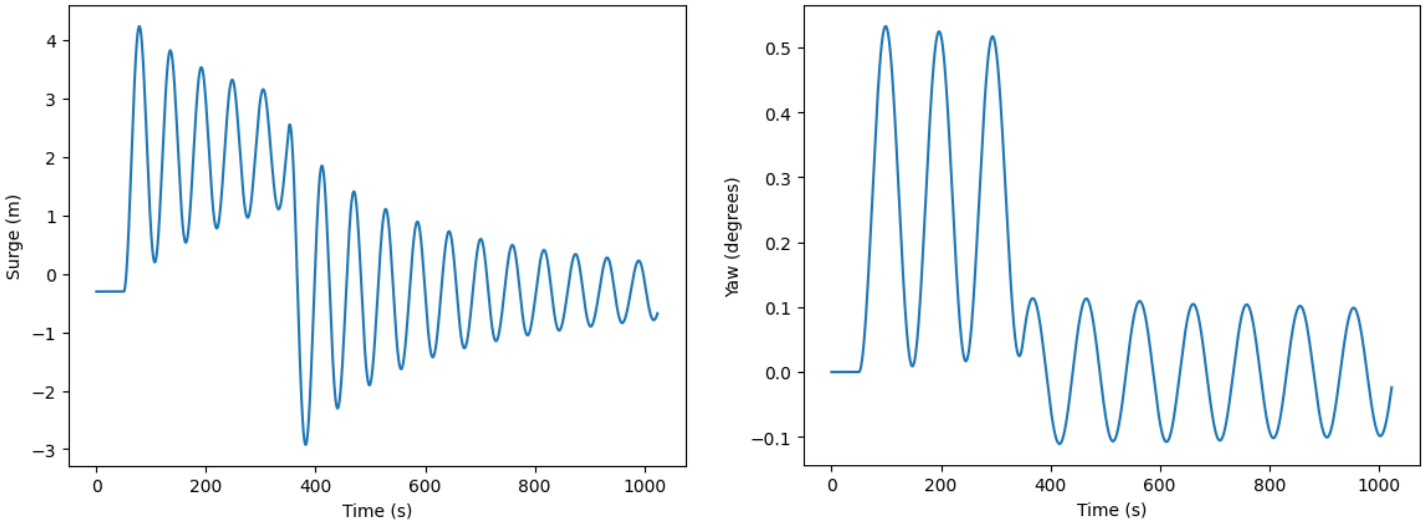

Figure 3.7 Decay test in Surge and Yaw.

3.7 Proposed systems natural periods

After validation of the model, we measured the natural periods of the platform in the 60-meter water depth. This was done for five different mooring system configurations with varying polyester and bottom chain lengths. The different mooring configurations all had the same

pretension. This was done to evaluate the changes in the natural frequencies of the system with varying mooring designs.

Table 3.6 presents the different mooring line configurations that were tested. For all of the tested models, the top chain was kept at a constant length of 50 meters. The anchor radius was also constant for all of the models at 1068 meters. The length of the polyester was first defined and the bottom chain was adjusted to reach the desired pretension value of 10% of MBS. With this approach, we only evaluate the effect of the polyester ratio of the mooring line, ie how much percentage of the whole line is made of synthetic rope, on its dynamic behavior. Figure 3.8 shows the visual presentation of the mooring line configuration without any environmental loads applied.

Table 3.6 Different Mooring System (MS) configurations with the same pretension.

Configuration	Bottom Chian length (m)	Polyester length (m)
MS1	200.0	754.9
MS2	306.0	650.0
MS3	407.0	550.0
MS4	508.2	450.0
MS5	609.5	350.0

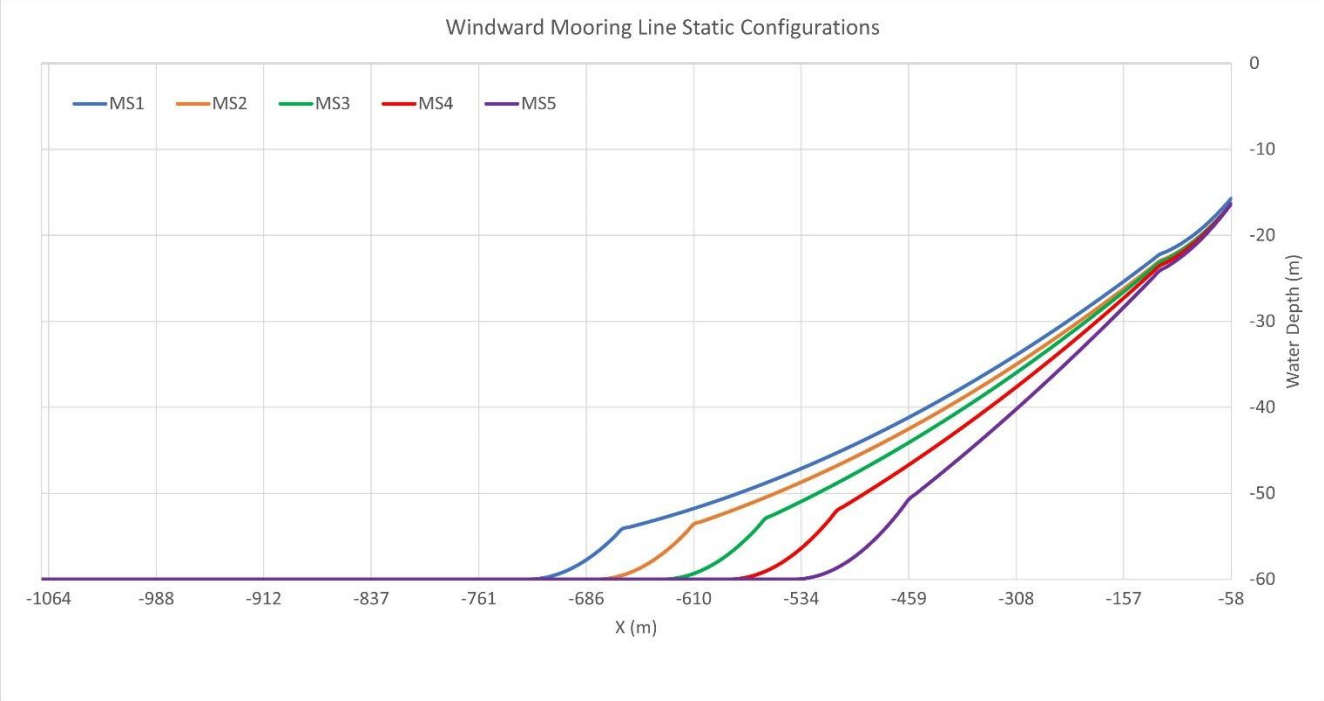

Figure 3.8 Static configuration of a windward mooring line in XZ plane.

3.8 System restoring forces

System restoring force is an important parameter in maintaining the platform stability. To measure this we need to evaluate the tension in the mooring lines as the function of the platform horizontal displacement. Several factors such as the angle of the mooring lines with the seabed, wave heading, and material properties can influence the restoring force. Previous research shows that the restoring force tends to decrease with a larger anchor radius and certain wave headings [50, 51]. Polyester mooring lines have been shown to exhibit better restoring capability [52].

In this study to measure the restoring force, varying horizontal forces were applied to the platform, and the displacement was measured. Finally, a polynomial curve was fitted to the measured data.

To assess the platform's maximum movements, it was subjected to extreme environmental conditions at the rated wind speed, with wave headings ranging from zero to 60 degrees in 15-degree intervals. The resulting displacements were then measured and plotted in what is known as the watch circle. The watch circle shows the safe distance from a floating structure that other vessels can get to.

3.9 Extreme response analysis

According to the American Bureau of Shipping (ABS), floating offshore wind turbines must withstand operational and environmental sea states at their site of installation. For this, the performance of the turbine at design load cases (DLCs) needs to be evaluated. DLCs are seastates with a reasonable probability of occurrence that need to be evaluated to measure the adequacy of platform and mooring system design [53]. Predicting the long-term extreme response, such as loads and displacement, of the floating offshore platform during the design stage is essential. Achieving this prediction typically involves extensive long-term analysis of all the sea states for the site of interest. This is the most accurate method but also highly inefficient due to the need for numerous computationally heavy simulations [54, 55].

To address this problem, several new methods have been proposed in recent years. One such method is the Environmental Contour Method (ECM). ECM improves efficiency by using only a small number of significant sea states. These sea states are located along environmental contours. The contour is a graphical curve that represents the extreme conditions that can occur over a certain period of investigation. All the points inside this area are points with higher probabilities of occurrence so we only need to evaluate the points on the circumference which

reduces the number of required simulations significantly. Figure 3.9 illustrates such an environmental contour in a two-dimensional space for wind speed and significant wave height [55].

Although the results of the ECM are generally accurate, it has been shown that for structures like wind turbines, which have different modes of operation at varying wind speeds (e.g., parked or operating), ECM can cause a discontinuity in the extreme responses for both states. To address this issue, a Modified Environmental Contour Method (MECM) was designed by Li et al. [55]. This method demonstrates improved accuracy in predicting responses under both parked and operating conditions. To understand the concept of MECM it is first necessary to explain the concept of First Order Reliability Method (FORM) and Inverse First Order Reliability Method (IFORM).

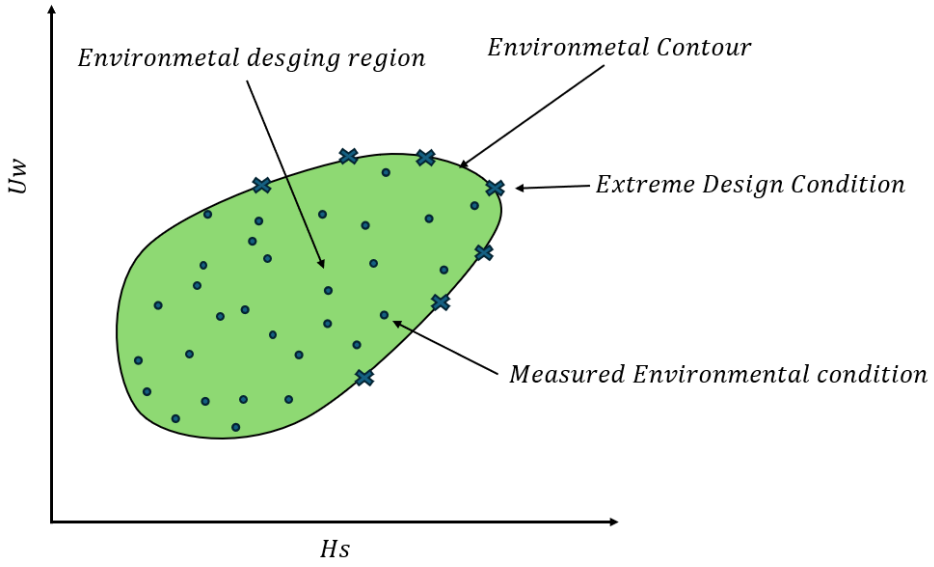

Figure 3.9 Environmental Contour method concept adapted form [54].

3.9.1 FORM, IFORM, and ECM

The Inverse First-Order Reliability Method (IFORM) is another efficient method for estimating extreme responses. ECM is based on the principles of IFORM, where it is not necessary to consider all environmental states, as only a few of these states lead to extreme responses. Both FORM and IFORM rely on the mathematical technique of transferring variables from physical space (X-space) to a standardized space (U-space). For instance, transforming the extreme response X, wind speed U_w, wave period T_P and significant wave height H_S into the U-space results in the variables U_X, U_{U_w}, U_{T_P} and U_{H_s} . This transformation, known as the Rosenblatt transformation, can be described by the following equation:

$$U_{U_w} = \Phi^{-1}\big(F(U_w)\big) \quad \text{(Equation 3.5)}$$

$$U_{H_s} = \Phi^{-1}\big(F(H_s \mid U_w)\big) \quad \text{(Equation 3.6)}$$

$$U_{T_P} = \Phi^{-1}\big(F(T_P \mid U_w, H_S)\big) \quad \text{(Equation 3.7)}$$

$$U_X = \Phi^{-1}\big(F(X \mid U_w, H_S, T_P)\big) \quad \text{(Equation 3.8)}$$

In which F is the cumulative distribution function (CDF) and Φ^{-1} is the inverse of the CDF of a normal distribution. Additionally, we can find the distance to the origin in the U-space as:

$$U = \sqrt{U_{U_w}^2 + U_{H_s}^2 + \ U_{T_P}^2 + \ U_X^2} \quad \text{(Equation 3.9)}$$

With the distance to the origin defined, we can determine the probability of exceedance as $1 - \Phi^{-1}(U)$. To find the extreme short-term t-hour response in N years return period and the associated sea states, we use the corresponding value for U:

$$U = \Phi^{-1}\left(1 - \frac{1}{\mathrm{N} * 365.25 * \frac{24}{\mathrm{t}}}\right) \qquad \text{(Equation 3.10)}$$

If, for simplicity, we consider only H_s and U_w as variables for the sea state along with the response, we end up with a three-dimensional space. In this space, the First Order Reliability Method (FORM) results in a sphere corresponding to the desired return period in the U-space, as illustrated in Figure 3.10. By using the Inverse First Order Reliability Method (IFORM), we can determine the extreme response of the sea states located only on the surface of the sphere, significantly reducing the number of sea states that need to be considered [55].

The Environmental Contour Method (ECM) is based on the same concept but simplifies the approach further by reducing one of the dimensions, specifically the response itself. This results in a two-dimensional contour representing the extreme conditions, thereby minimizing the number of required simulations even more effectively. Figure 3.11 shows the contour of the ECM derived from Figure 3.10. By implementing the ECM, the largest response along the contour is considered the extreme response for the respective return period. As can be seen, both methods provide comparable results regarding the sea state that results in the extreme response [55].

3.9.2 Modified Environmental Contour Method (MECM)

As previously mentioned, one of the drawbacks of the ECM is when wind turbines operate under different conditions, such as parked state and in operation state. To overcome this limitation, the Modified Environmental Contour Method (MECM) was proposed. With MECM, an additional environmental contour for the cutout speed is considered to remove the discontinuity between these two operational states. This phenomenon can be seen in Figure 3.12. This illustrates that while the ECM method predictions can deviate from those of the comprehensive IFORM method, MECM provides accurate predictions while still maintaining efficiency by reducing the necessary number of sea state evaluations [55].

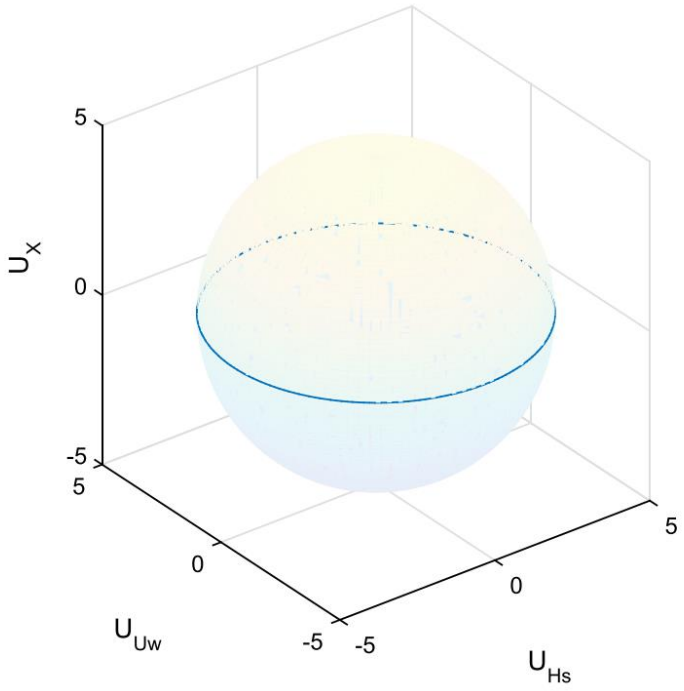

Figure 3.10 The 50-year return period contour for extreme response with respect to significant wave height and wind speed reproduced from [55].

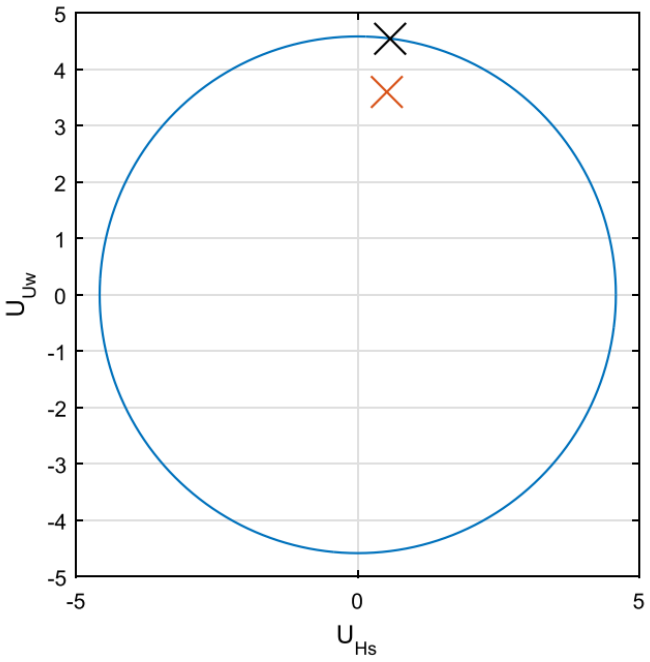

Figure 3.11 Comparison of the extreme response from ECM (black cross) and IFORM (red cross) method results reproduced from [55].

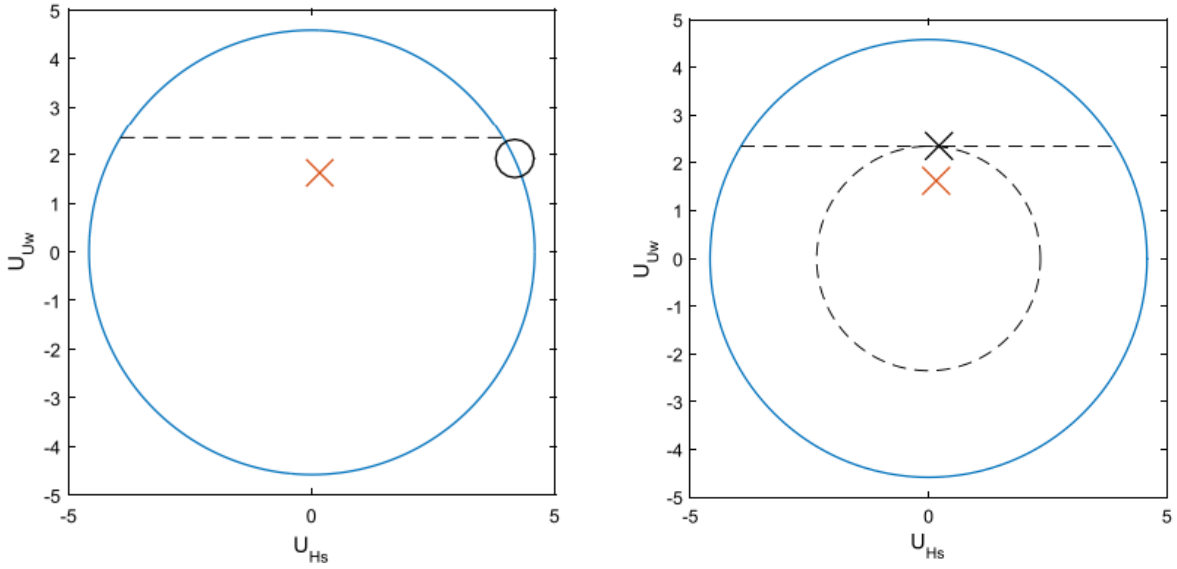

Figure 3.12 The comparison between ECM (left) and MECM (right) for extreme state. The horizontal dashed line represents the U-space value for the cutout wind speed, while the red cross denotes the IFORM extreme sea state. In MECM, the dashed circle represents the cutout speed contour, resulting in a prediction closer to IFORM compared to solely considering the contour for the return period (blue circle). Reproduced from [55].

3.10 Fatigue Analysis

The fatigue phenomenon is described as the accumulation of damage in the material under cyclic loading over a specific period. Each cycle of loading causes a certain amount of crack growth and propagation that contributes to what is known as fatigue damage. Fatigue damage accumulation can occur at stresses well below the ultimate tensile stress or yielding stress of materials hence making it a serious cause of failure in many different industries. In each cycle of loading the cracks that start on the materials surface or a defect grows gradually until it reaches a critical length which causes a sudden failure at this point. Fatigue analysis is a method that is developed to estimate the fatigue damage accumulation and life span of components in a quantifiable manner. Fatigue analysis is a critical part of operation and maintenance which helps to predict the life span of equipment and prevent catastrophic failures [56, 57].

Fatigue happens in two stages. The first stage starts with crack formation at the material surface, typically as cracks on crystallographic slip planes. In the second stage, the crack grows in a direction normal to the applied load. This process can be observed in Figure 3.13, where the crack initiates at one corner of a chain (Top part of the picture). As it progresses through the cross-section of the mooring chain, it forms distinct lines at each stress which are known as beach marks [57].

Figure 3.13 Fatigue crack growth and beach marks formation on a mooring chain cross section reproduced from [57].

Like other industries, fatigue is one of the main failure problems of the offshore industry as well. As the environmental loads offshore cause cyclic and random loading on the mooring lines, fatigue analysis becomes a crucial part of their design and maintenance. Fatigue analysis can be measured with two different methods. The first method involves utilizing stress cycles (SN curves) or tension cycles (TN curves), which are based on determining the number of cycles a component can withstand under a specific stress or load range before failure occurs. The second method relies on fatigue crack growth models, which predict failure if cracks reach a critical length. Although the latter approach offers better accuracy, it's not a useful method as it is difficult to measure crack length especially in the offshore industry, making it less practical. Consequently, SN or TN curves are mainly used in the industry for fatigue analysis [57].

3.10.1 Miner's rule

The Miner's rule, which is also known as Palmgren-Miner's rule, is a linear method for fatigue damage accumulation. Initially proposed by Palmgren and then Miner suggested a mathematical formula for it. The rule is represented mathematically as follows:

$$D = \sum \frac{n_i}{N_i} \qquad \text{(Equation 3.11)}$$

Here, D denotes the annual accumulated damage and failure occurs when D reaches a value of 1, n_i represents the number of times when the component undergoes a specific tension range, and N_i is the total number of cycles the material can withstand before failure under the mentioned tension range [58].

To determine the value of N_i we utilize the SN curve, which follows the Basquin equation provided below:

$$N_i = \frac{a}{S^m} \qquad \text{(Equation 3.12)}$$

Here, S represents the stress range experienced by the component, while m and a denote the intercept and slope of the logarithmic form of the SN curve, respectively. These parameters are derived from experimental tests.

In some cases, the TN curve is implemented instead of the SN curve which follows a similar equation with the difference of using tension range normalized by the mean breaking strength instead of stress range:

$$N_i R^m = a \quad \text{(Equation 3.13)}$$

$$R = \frac{\Delta T}{MBS} \quad \text{(Equation 3.14)}$$

Table 3.7 shows the recommended values for some of the common materials for mooring lines by different standards.

Table 3.7 SN and TN curve parameters suggested by DNV GL and API. Adopted from [57].

	DNV GL (SN Curve)			API (TN curve)	
Component	**a**	**m**		**a**	**m**
Stud chain	1.2e11	3.0		1000	3.0
Studdles chain	6.0e10	3.0		316	3.0
Polyester	-	-		25000	5.2

To estimate the design life, we can calculate 1/D which should exceed the desired service life. This is usually done considering a safety factor. It's important to note that while Miner's rule is widely used in fatigue analysis for the offshore industry, it does not account for the sequences the loads are applied. Nevertheless, it remains the recommended approach by relevant standards such as the American Petroleum Institute (API), the American Bureau of Shipping (ABS), Det Norske Veritas, Germanischer Lloyd (DNV GL), and others [57].

3.10.2 Time domain fatigue analysis

Fatigue analysis can be performed either in the time domain or frequency domain. As the names imply the time domain is based on the time series of tensions or stress that the component

has experienced. In this method, the number of cycles that the component has experienced is counted and the fatigue damage is calculated. For the frequency domain analysis, we use the power spectral density (PSD) of the tension or stresses to estimate the fatigue damage. The use of time domain fatigue analysis over frequency domain analysis is much more computationally expensive as it requires long time domain simulations to be carried out and then we use the time history of tensions to measure the accumulated damage. The longer the simulation the more accurate the results are. The frequency domain on the other hand is a much faster analysis but with the drawback of less accuracy to capture all the stress cycles [59]. As we are going to use the time domain fatigue analysis in this thesis, we are not going to explain the frequency domain fatigue analysis in this thesis.

To assess the time domain fatigue damage in the platform and mooring lines, we employ a technique known as rainflow counting. This method was first introduced by Matsuishi and Endo. The rainflow counting method involves rotating the time history diagram by 90 degrees so that time becomes the vertical axis, pointing downwards. To conduct rainflow counting, we visualize each peak or valley in the time history diagram as the starting point for a raindrop, which then follows a path downward similar to rain falling down a series of roofs forming paths along its way. The drops continue until the next valley has a lower magnitude than the beginning or the path is blocked by the previously formed paths (Figure 3.14). Each of these paths represents a half cycle, with the tension range corresponding to the projection of the path on the tension axis from the minimum to maximum tension or stress. In the end, all cycles with the same tension range are counted and stored in a rainflow matrix, which is then used to quantify the fatigue damage caused by each stress range over the time history.

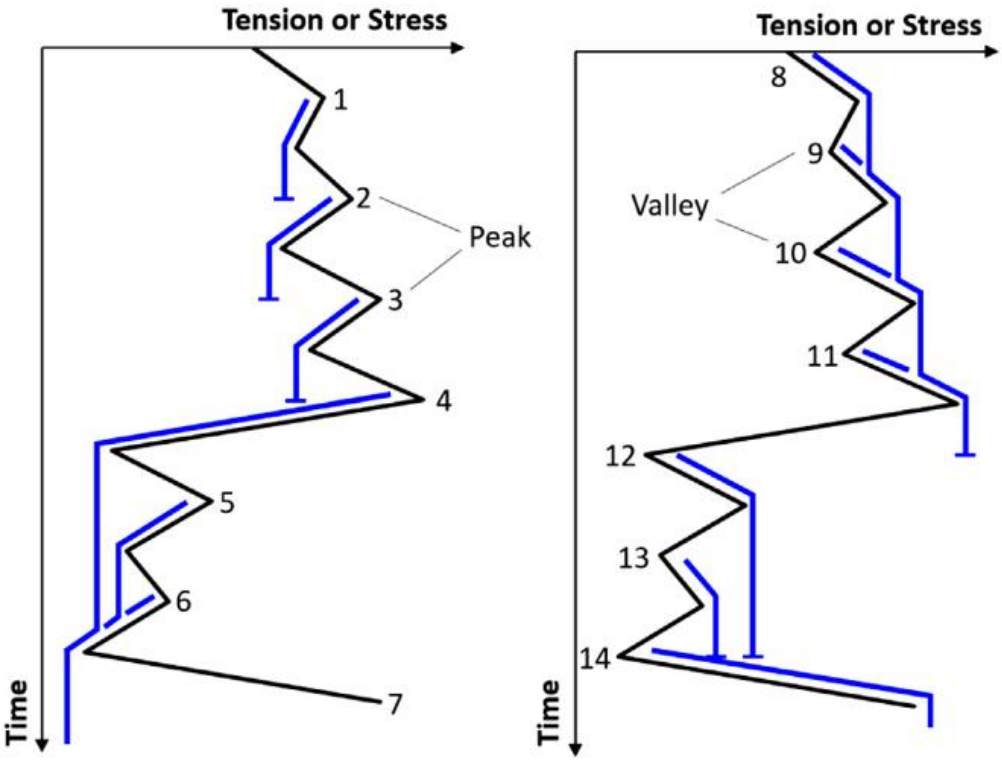

Figure 3.14 Rainflow counting algorithm by Matsuishi and Endo. Reproduced from [57].

In addition to the Matsuishi and Endo method, there are alternative approaches to rainflow counting, including the Three Point Method and the Four Point Method. In our study, we utilized the Four Point Counting Method to analyze the fatigue damage in the platform and mooring lines [58].

3.10.3 Four-point counting

The Four Point Counting Method examines four consecutive peak and valley points in the time series data. If the load range between the two inner points is smaller than the load range

between the two outer points, ie the load range of the inner points is encompassed by the load range of the outer points, then one cycle between the two inner points is counted. The two inner points are then removed from the time series, and the process continues until all points are evaluated. This approach can be easily implemented for real-time data monitoring, such as in digital twin technologies used for fatigue analysis [58, 60]. Figure 3.15 illustrates the concept of four-point counting. One drawback of this method is the residuals that remain for the points that do not satisfy the criteria for cycle counting. These residuals may need to be included in the damage calculation, as they could contribute to the overall fatigue damage accumulation [58]. The Python code for the four-point counting method is provided in Appendix A.

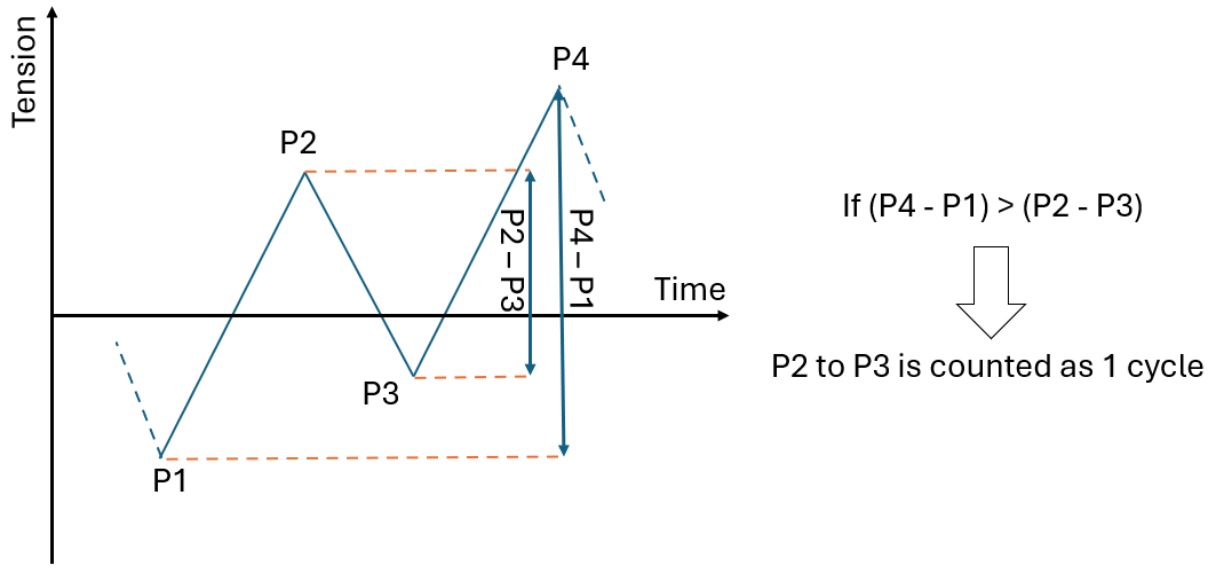

Figure 3.15 Four-point counting method.

3.11 Environmental bin selection

For every site of interest, measurements of significant wave height (Hs), wave period (Tp), and wind speed are required. Additionally, it is crucial to understand the probability of each of these sea states occurring. To estimate these parameters for the Sørlige NordSjø II site (Figure 3.16), we employed the joint distribution derived by Cheynet et al. [28]. This site shows great promise for the implementation of an offshore wind park.

According to Cheynet et al.'s [61] work to derive the joint distribution, a conditional modeling approach was used with a temporal resolution of 3 hours. The joint distribution is expressed in the following form:

$$f_{H_s,\overline{\overline{U}}_{hub},T_p}(h,u,t) = f_{H_s}(h).f_{\overline{\overline{U}}_{hub}|H_s}(u|h).f_{T_p|H_s}(t|h) \quad \text{(Equation 3.15)}$$

Where the joint distribution $f_{H_s,\overline{\overline{U}}_{hub},T_p}(h,u,t)$ is measured by the multiplication of the marginal distribution H_S, and two conditional distributions of $\overline{\overline{U}}_{hub}$ and T_p for the given H_s.

To make it more clear, the marginal distribution of H_s presented as $f_{H_s}(h)$ represents the probability distribution of significant wave heights. The conditional distribution $f_{\overline{\overline{U}}_{hub}|H_s}(u|h)$ represents the probability of wind speed $\overline{\overline{U}}_{hub}$ given a specific significant wave height H_s. Similarly, the conditional distribution $f_{T_p|H_s}(t|h)$ is the probability of a wave period T_p given H_s.

By the use of this joint distribution for the SN II site, we make sure that the inter-dependencies are these sea state parameters to each other are considered.

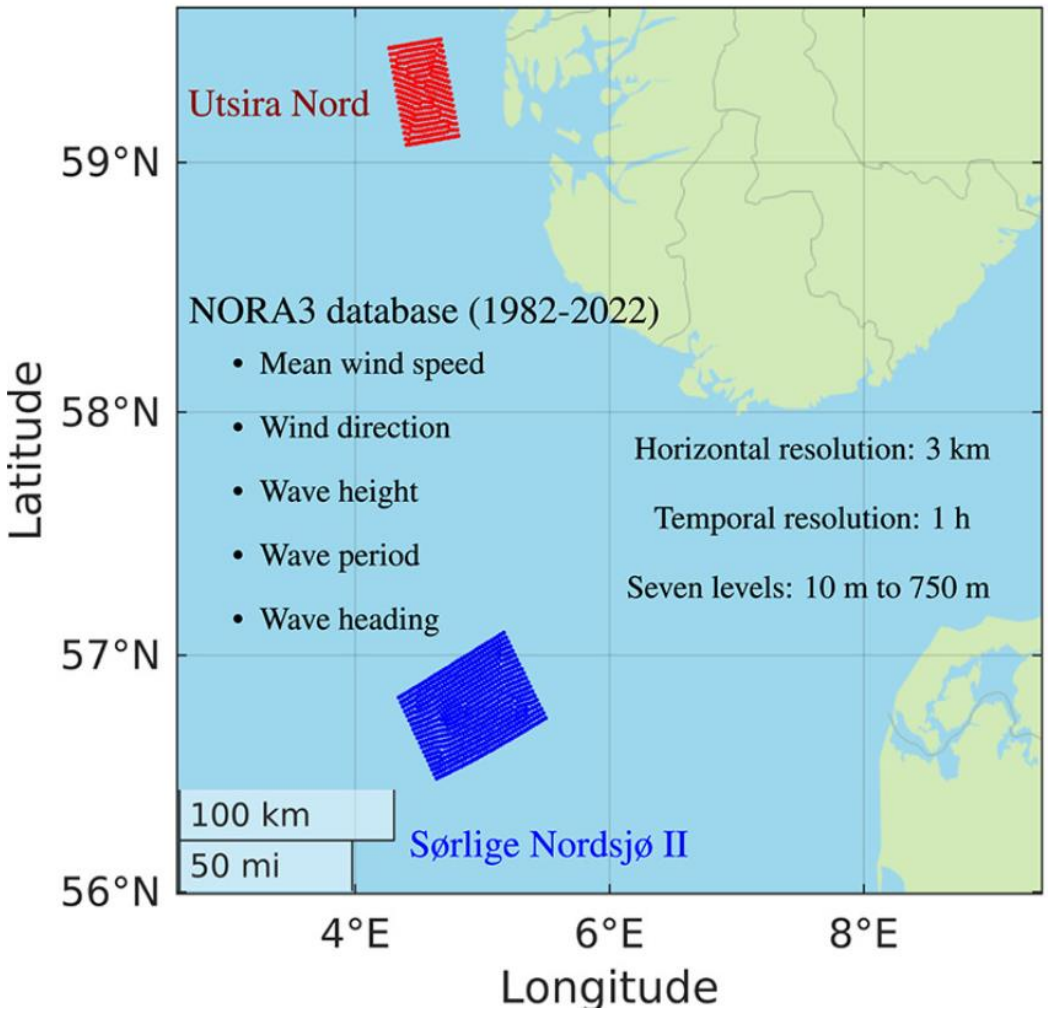

Figure 3.16 Location of Sørlige Nordsjø and Utsira Nord as two promising wind farm development sites. Reproduced from [49].

In this study, 1 million random sea states were derived according to the joint distribution for the SN II site. Subsequently, a maximum dissimilarity algorithm was developed (based on the procedure described in Kanner et al.'s [61] work) to generate 20 representative sea states that are as distinct as possible while encompassing the entire range of long-term sea states for this site.

3.12 Maximum dissimilarity algorithm

The Maximum Dissimilarity Algorithm (MDA) is a method used to select groups of data from a larger dataset while ensuring that the selected data points are as dissimilar as possible to each other. In this method, clusters of points are formed and their average is representative of the whole data points in those clusters. This is done in a way to represent the entire dataset in a more compact form. The advantage of this method is its ability to eliminate user bias in data selection and reduce the dataset to a manageable size for further investigation. This method was initially developed for use in biotechnology and drug discovery. MDA was employed to select different compounds from a vast selection of chemicals that can be combined to form new substances. MDA algorithm simplifies and also automates the screening and generation of new substances. It is also worth mentioning that this method is computationally heavy as it is a $O(N^2M)$ algorithm and there are methods to make it more efficient but we have used the traditional approach to implement the code in this study (Appendix B) [61].

The same approach for environmental bin selection is implemented in this study. The MDA algorithm was used to select significant wave heights (H_s), wave period (T_p), and hub-height wind speed (U_w) from large datasets (1 million sea states) made from the joint distribution explained in the previous section. This is to create a smaller number of representative sea state clusters. The average of sea states in each cluster represents all of the sea states in that cluster. The probability of each sea state was estimated based on the number of sea states within each cluster to the total number of sea states generated based on the joint distribution.

Figure 3.17 illustrates the procedure of the Maximum Dissimilarity Algorithm (MDA) flowchart. The initial step in MDA is data normalization, which scales all of the variables between

0 and 1. Subsequently, the two data points with the greatest distance between them are identified and the initial clusters are made with points that have a lower distance to them than the defined distance tolerance. The lower the distance tolerance the more clusters are going to form and the higher the quality of the MDA results. But this will be at the cost of more simulations.

The next step is to measure the distance between each non-clustered point and all existing cluster centroids. The point with the maximum distance from any cluster centroid is selected to form a new cluster creation point. Points within the specified tolerance distance of this new cluster creation point are added to the cluster. This process is continued until all points are assigned to the new clusters, or the desired number of clusters is achieved. In the latter case, the remaining points are assigned to their nearest cluster, and all cluster centroids are updated accordingly. In this study, the MDA code is designed to continue forming clusters until all points are assigned, ensuring comprehensive coverage of the data set. In the last step, all the data are denormalized again to show the original values. Figure 3.18 also shows the graphical representation of MDA algorithm cluster creation in 2D space [61, 62].

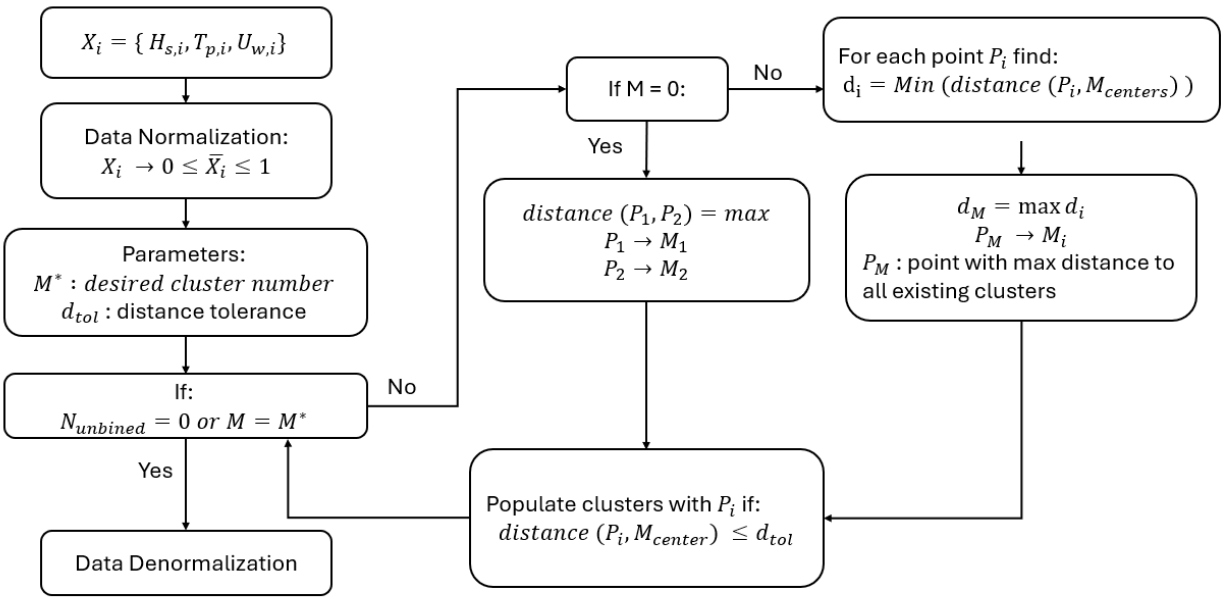

Figure 3.17 Flowchart representation of MDA algorithm. Adopted from [61].

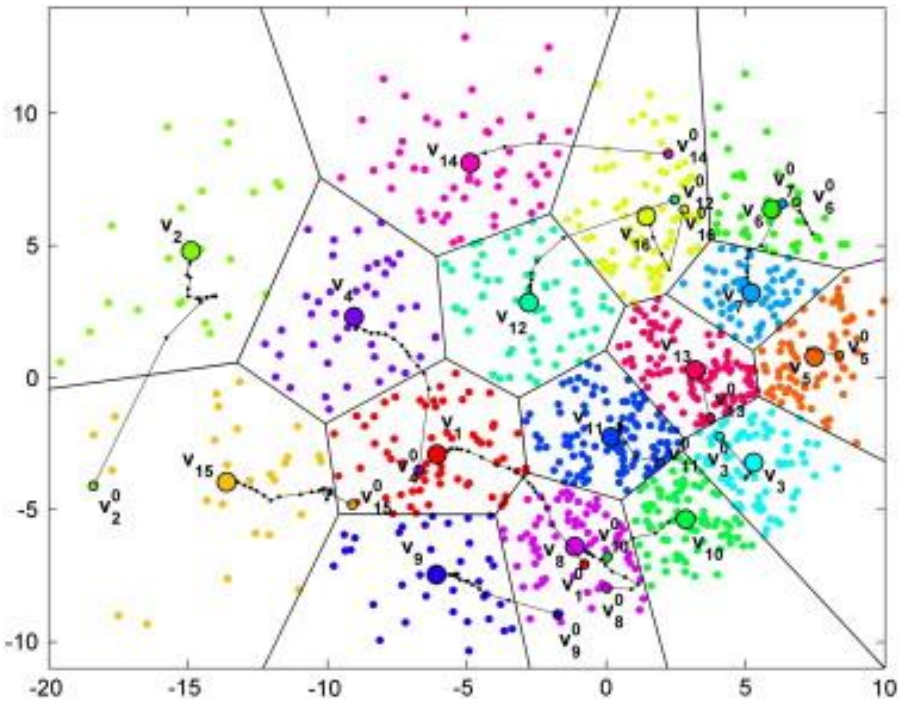

Figure 3.18 Schematic representation of MDA algorithm in 2D space. Reproduced from [62].

Figure 3.19 demonstrates the results of the Maximum Dissimilarity Algorithm (MDA) with a high distance tolerance. This results in the creation of only four clusters and is only used here for demonstration purposes. In this study, the distance tolerance was reduced until the formation of 20 clusters, and the quality of the clusters was assessed.

To evaluate the representative bins' quality, the quality metric q was defined based on Kanner et al.'s [61] work. This quality metric is presented in percentage. If the number of clusters approaches the number of generated data points or in other words, the distance tolerance decreases the quality of the selected bins increases.

This quality metric is defined as:

$$q = 100 * \left(1 - \frac{\overline{D}}{M^*}\right) \quad \text{(Equation 3.16)}$$

where $\overline{D}$ is the average distance of the points in each cluster from cluster centroids, and M^* is the number of centroids. Notice that this quality metric is used solely for comparing the effectiveness of cluster creation and has not been tested to determine if it results in more accurate fatigue damage calculations [61].

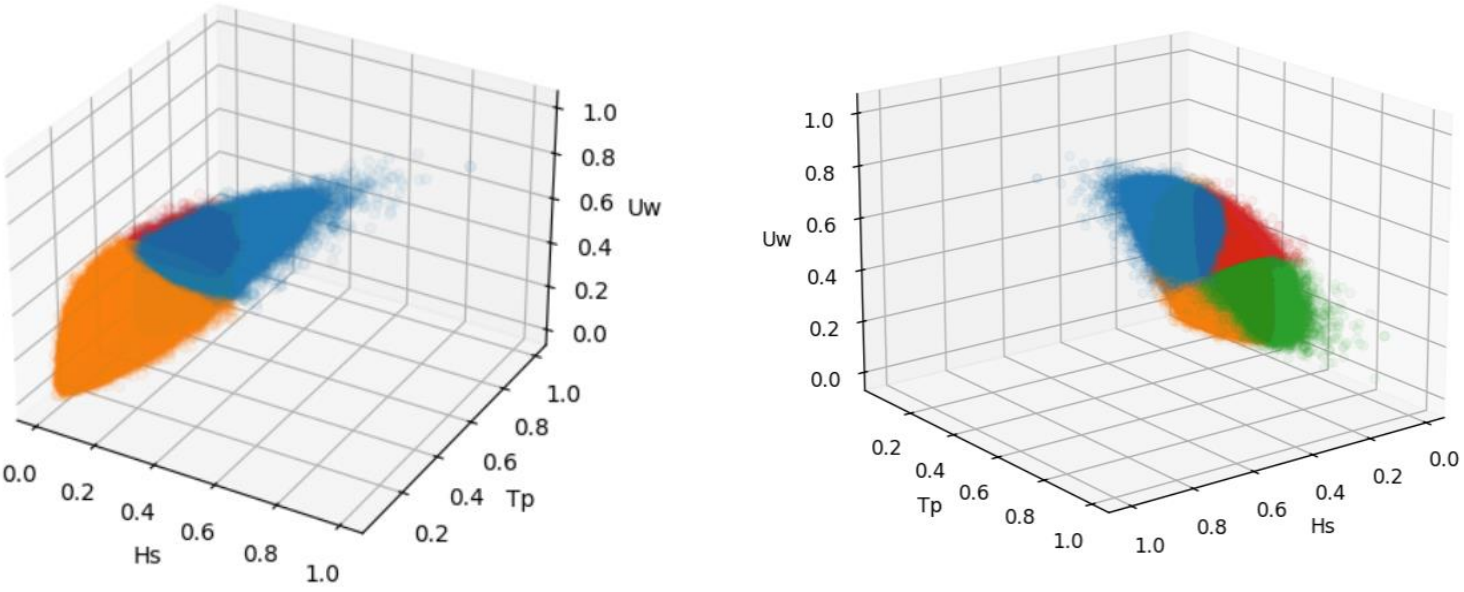

Figure 3.19 The normalized results of the maximum dissimilarity algorithm from different angles which resulted in only 4 clusters from a total of 1 million data points.

4 Results and Discussion

4.1 Validation

The results of the decay test are summarized in Table 4.1. It is evident that the natural frequencies in all degrees of freedom closely correspond to those of the reference model. Additionally, the comparison of RAO in the surge, heave, and pitch between the reference model and the proposed model is depicted in Figure 4.1, Figure 4.2, and Figure 4.3 respectively. The RAO exhibits a similar trend to that of the reference model. This alignment serves to validate not only the proposed model but also the derived natural periods across varying depths and mooring configurations.

Table 4.1 Comparison of the natural frequencies between the Reference floater (VolturnUS-S) and the proposed model at a depth of 200 meters.

Degree of freedom	Reference Model (Hz)	Proposed Model (Hz)
Surge	**0.007**	**0.007**
Sway	**0.007**	**0.007**
Heave	**0.049**	**0.049**
Roll	**0.036**	**0.035**
Pitch	**0.036**	**0.035**
Yaw	**0.011**	**0.011**

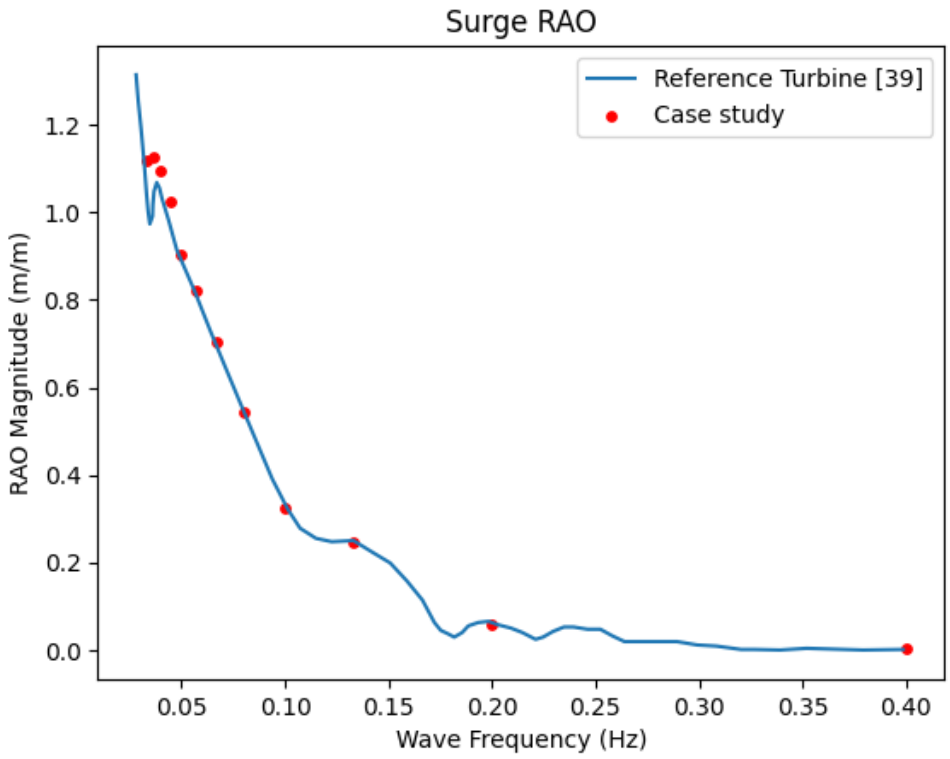

Figure 4.1 Surge RAO comparison against the reference wind turbine.

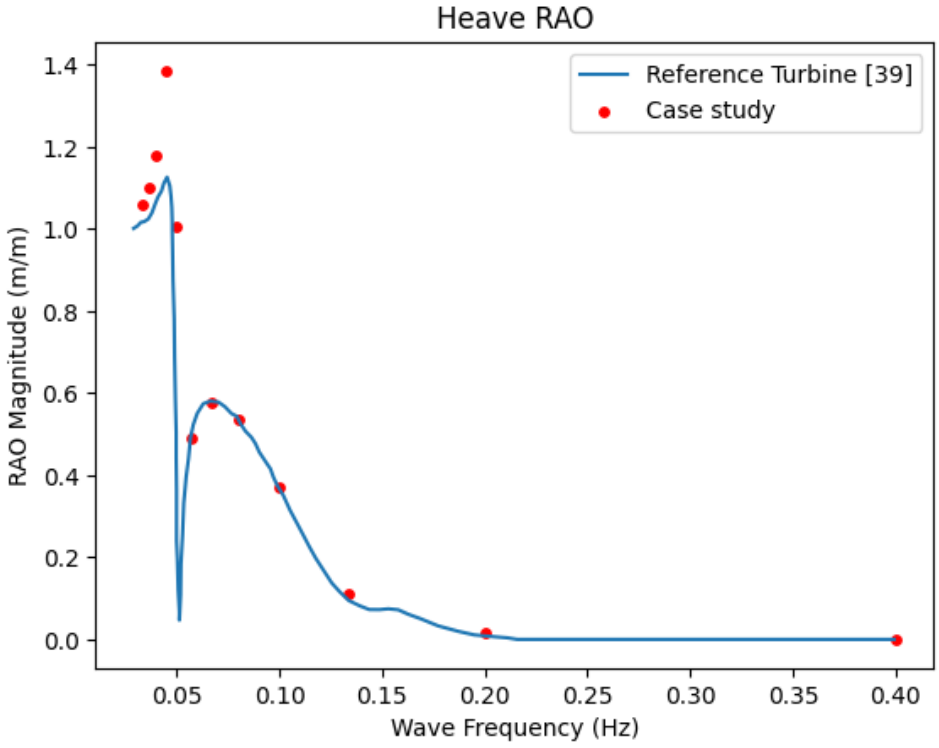

Figure 4.2 Heave RAO comparison against the reference wind turbine.

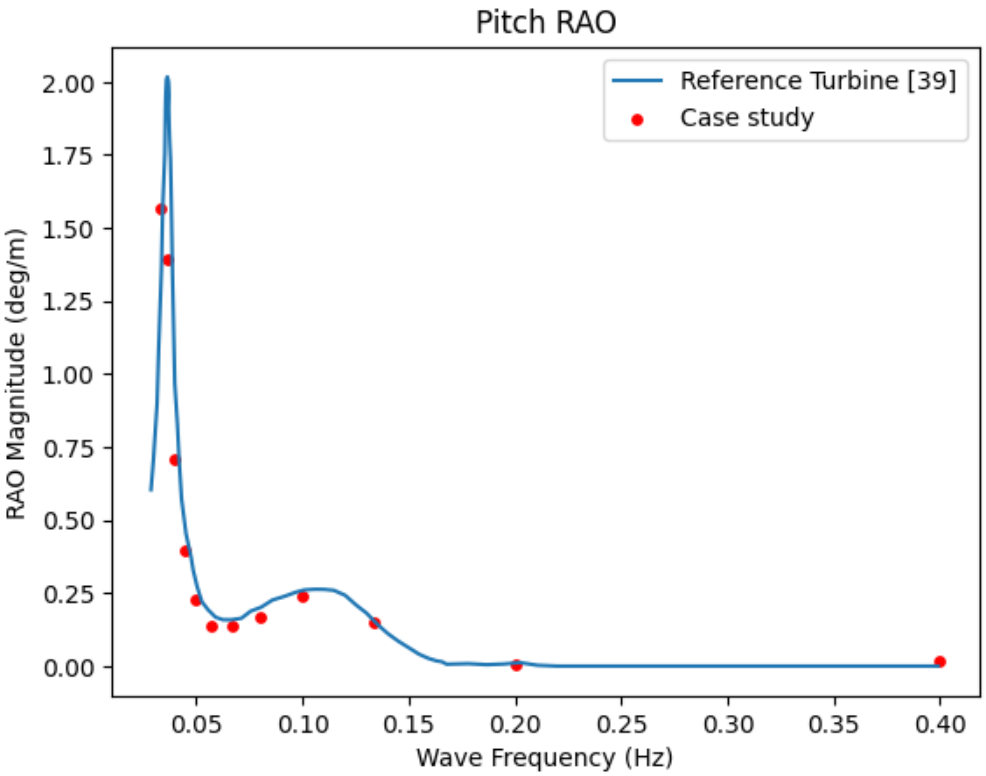

Figure 4.3 Pitch RAO comparison against the reference wind turbine.

4.2 Proposed systems natural periods

The results of the numerical free decay tests conducted for the proposed platform, both at a depth of 200 meters and across various configurations at 60 meters, are illustrated in Figure 4.4. As anticipated, the natural periods of the supporting platform in heave, roll, and pitch demonstrate consistency across various water depths. Additionally, the natural period in yaw remains relatively unaffected by changes in depth, owing primarily to the influence of mooring pretension [13]. However, noteworthy reductions are observed in the natural periods of surge and sway in shallower waters, attributable to the heightened stiffness of the system resulting from the decrease in water depth.

Additionally, it can be observed that the natural periods in all degrees of freedom, except surge and sway, remain consistent across the various mooring configurations. However, the natural periods in surge and sway exhibit a noticeable decrease as the length of the polyester rope is reduced. This behavior was anticipated, as decreasing the length of the polyester rope results in an increased length of the bottom chain segment, consequently leading to a stiffer mooring system primarily influenced by the more rigid chain segment (Figure 3.8).

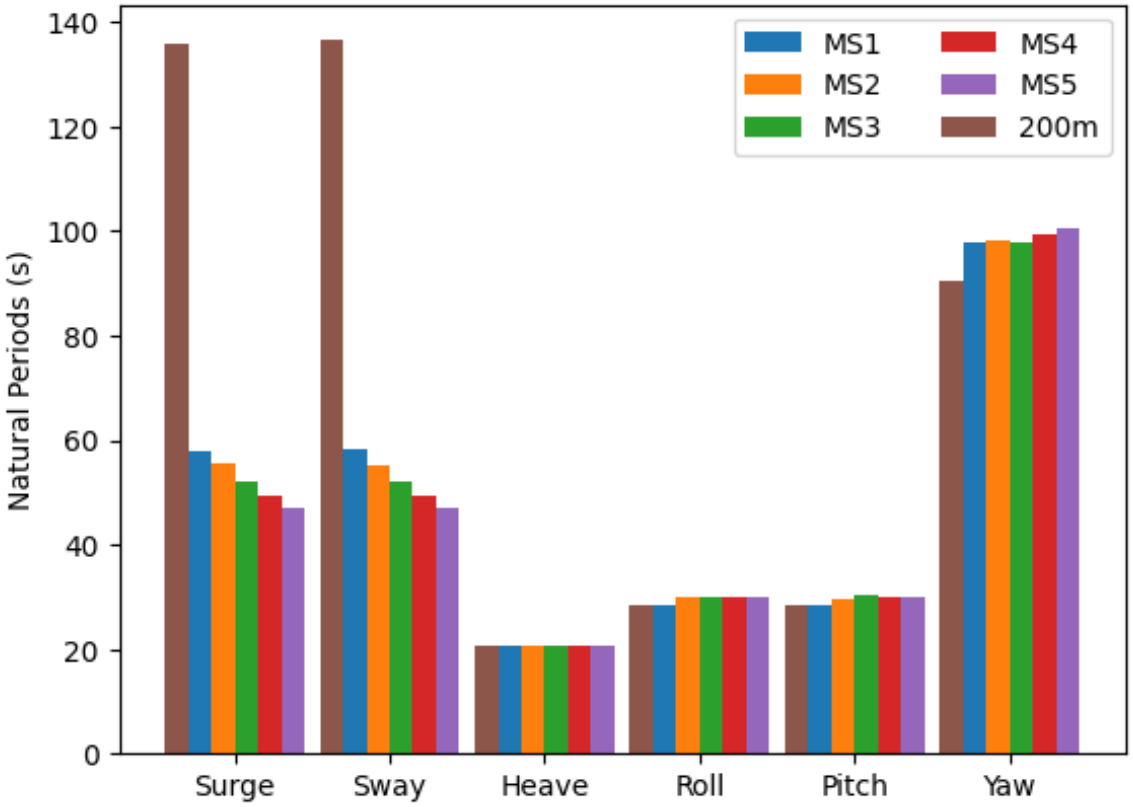

Figure 4.4 Comparison of the natural periods of the platform with different mooring system configurations at 60 meters depth with the reference platform at 200 meters depth.

4.3 System restoring forces

Figure 4.5 illustrates the variation in restoring forces of the different mooring line systems. As can be seen the polyester rope length reduction results in an increase in the restoring force. This behavior is due to the increased length of the stiffer chain segment, thereby increasing the platform's restorative forces. Moreover, it is noteworthy that the mooring system's restoring capability varies based on its chain/polyester length to total length ratio. Specifically, a system that is mainly composed of polyester exhibits lower restoring forces compared to the ones dominated by the chain. Therefore, not only does the length of the polyester rope influence the restoring force but also affects the overall stability of the platform.

Furthermore, Figure 4.6 shows the platform's horizontal movement around its center (watch circle) for different mooring configurations which is known as the watch circle. Configurations with longer lengths of polyester exhibit larger movement areas.

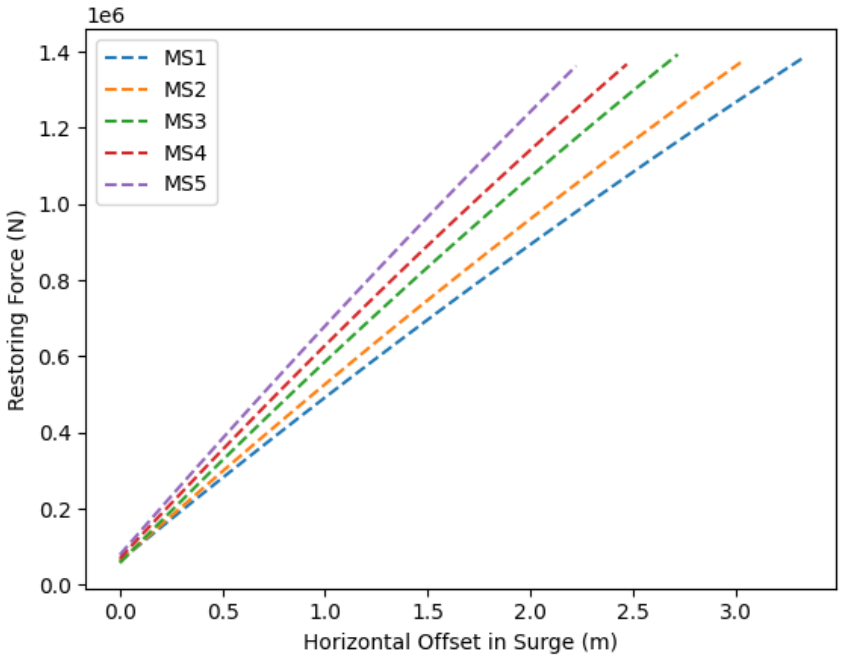

Figure 4.5 System restoring force for different mooring system configurations.

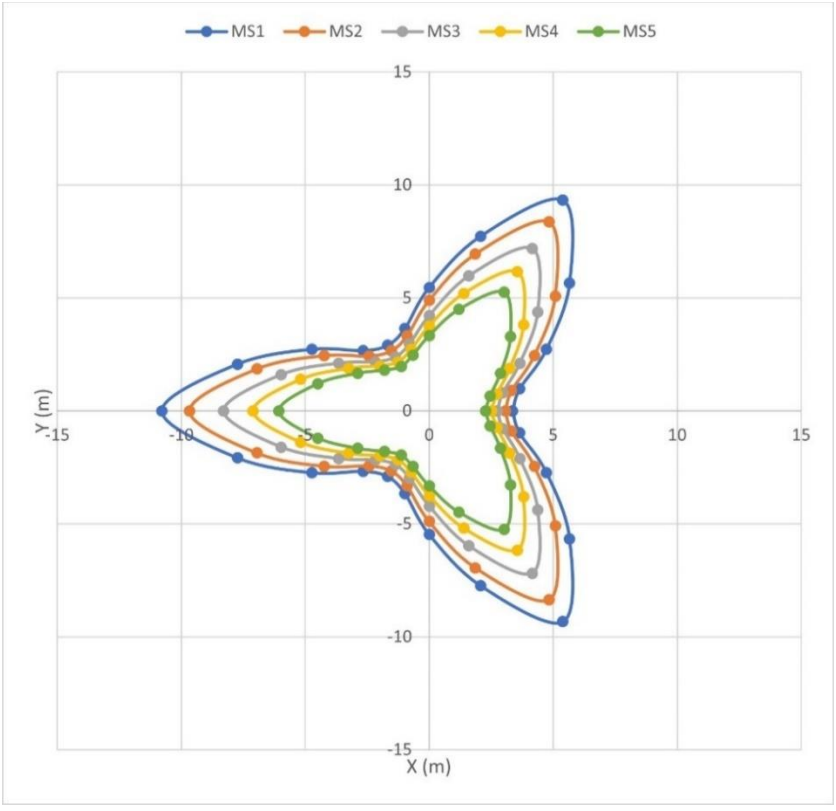

Figure 4.6 The Watch Circle for different mooring system configurations.

While increasing the chain segment length results in more stable platform movement and a smaller watch circle, it has been observed that the maximum tension in the mooring lines increases for shorter polyester configurations. Additionally, the standard deviation of the tension also rises similarly. This indicates that although the MS5 configuration provides a more stable platform, it is more reasonable to choose MS1. The reduced maximum loads on the mooring lines in MS1 would result in better performance concerning fatigue damage, as fatigue damage is correlated with load range amplitude, which is related to the standard deviation of the load.

Table 4.2 summarizes the maximum mooring line tensions and their standard deviations across different heading angles, while Figure 4.7 illustrates the time histories of the tension in the windward mooring line at a heading angle of zero degrees for both the MS1 and MS5 configurations. The maximum tension and the standard deviation of the tension in the mooring lines increase as the polyester rope length decreases. For example, the maximum tension in mooring line number 1 increases by more than 12% from MS1 to MS5, and the standard deviation increases by approximately 35%. This trend is also observed in the two leeward mooring lines (Table 4.3). Figure 4.7 shows that the tension range and variation in MS1 are encompassed by those in MS5, indicating lower maximum tension and lower standard deviation with longer polyester ropes.

Table 4.2 Statistics of the mooring line 1 tension for different mooring configurations at different heading angles θ.

	Stats	MS1	MS2	MS3	MS4	MS5
$\theta = 0$	Max	3.88E+06	4.00E+06	4.19E+06	4.30E+06	4.43E+06
	Std	4.43E+06	4.50E+06	4.63E+06	4.80E+06	4.98E+06
$\theta = 30$	Max	4.43E+06	4.50E+06	4.63E+06	4.80E+06	4.98E+06
	Std	3.74E+05	3.91E+05	4.09E+05	4.32E+05	4.68E+05
$\theta = 60$	Max	3.23E+06	3.27E+06	3.39E+06	3.54E+06	3.65E+06
	Std	2.25E+05	2.41E+05	2.57E+05	2.74E+05	2.63E+05

Table 4.3 Statistics of the leeward mooring lines tensions for different mooring configurations for the heading angle $\theta = 0$.

	Stats	MS1	MS2	MS3	MS4	MS5
Mooring 2	Max	1.03E+06	1.07E+06	1.11E+06	1.14E+06	1.18E+06
	Std	7.01E+04	7.79E+04	8.88E+04	9.95E+04	1.11E+05
Mooring 3	Max	9.86E+05	1.01E+06	1.07E+06	1.10E+06	1.11E+06
	Std	6.90E+04	7.60E+04	8.66E+04	9.65E+04	1.06E+05

The results from the different mooring configurations indicate that mooring systems with longer polyester ropes exhibit lower maximum tension and standard deviation, albeit at the expense of a larger watch circle area. Consequently, we decided to perform the fatigue analysis solely for the MS1 configuration in the final part of this study.

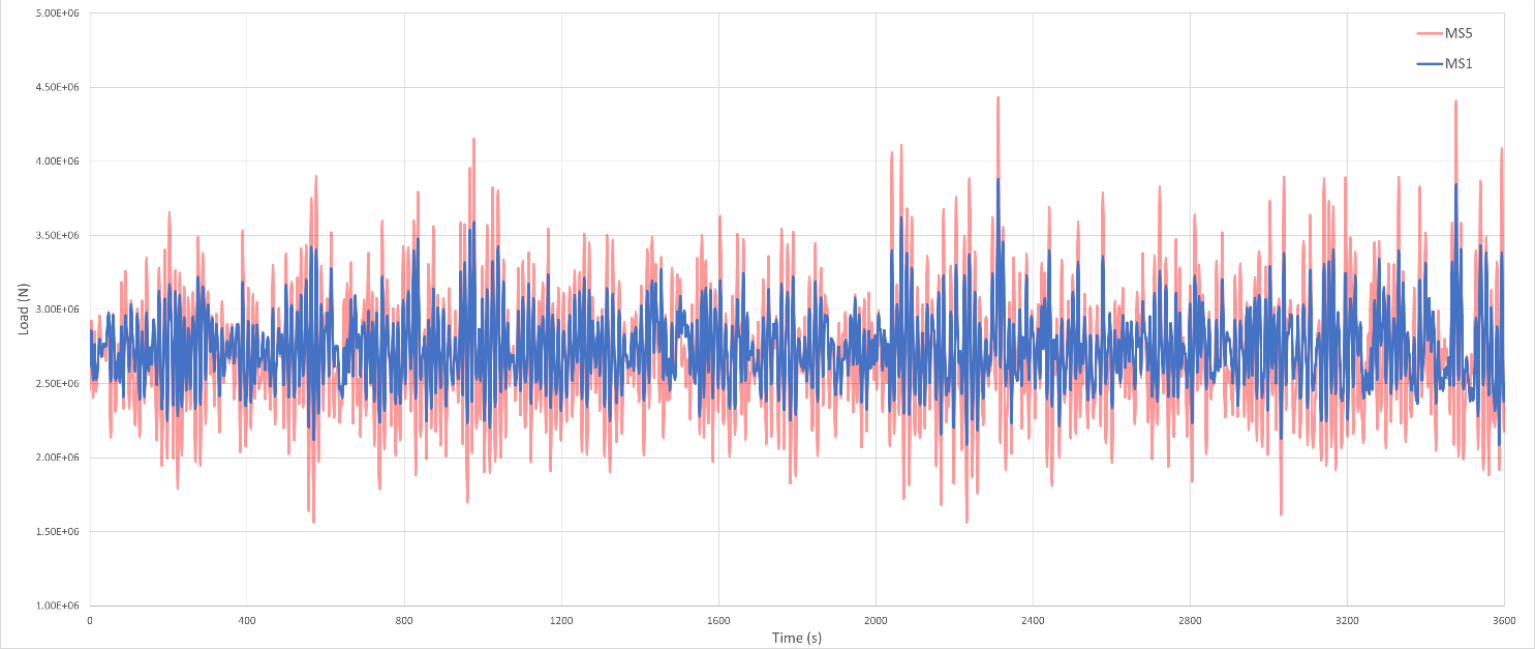

Figure 4.7 Comparison of the load time series for the windward mooring line between mooring system configuration 1 and mooring system configuration 5.

4.4 Motion responses

In this thesis, 23 environmental conditions were selected for the fully coupled time domain simulation. These sea states are presented in Table 3.4. The 3-hour platform response to these sea states was analyzed and the motion statistics consisting of mean, standard deviation, and maximum were presented.

Figure 4.8 and Figure 4.9 show the transitional and rotational power spectral density (PSD) graphs for each degree of freedom for the DLC16 sea state. A peak response can be seen around the natural frequency of the platform in these graphs. The natural periods of each DOF are presented in Table 4.1. It is worth noting the peaks in this simulation are not always the largest

response at the natural frequencies as there are peaks in response around wave and wind frequencies.

As can be seen, the sway response at the wind frequency is larger than its response at its natural frequency of 0.13 rad/s. The surge response at its natural frequency of 0.13 rad/s is also not as significant as its response at the wave frequency. This is while the heave response is comparable for both its natural frequency and wave frequency.

When it comes to the pitch and yaw response of the platform the response peaks at the platform's natural periods of 0.2 rad/s and 0.06 rad/s in each DOF. This suggests that the response in these DOFs is mainly dominated by the natural frequency of the platform. The roll motion on the other hand shows a more significant response at the wind frequency which shows the significance of aerodynamic loads for the roll dynamic behavior in this platform design.

As can be observed from these results the natural period response is not always the most significant for each platform as the wind and wave frequencies can show a more intense response due to the design of the platform.

In Figure 4.10, the surge response of the platform is depicted for a selected number of sea states. As was expected, surge displacement increases with the increase in wind speeds, peaking at the turbine's rated wind speed of 10.59 m/s during DLC16. By further increasing the wind speed, a decrease in surge displacement occurs due to the controller systems feathering the blades to reduce the aerodynamic loads. It is worth noting that DLC61, which represents the extreme 50-year conditions, exhibits a substantial surge displacement compared to EC21, although staying below the surge displacement observed at the extreme conditions observed at rated wind speed. This is due to the current presence in the extreme load cases at DLC61 and DLC16. The maximum

surge displacement response of the platform for DLC61 surpasses that of DLC16, which shows its importance for extreme response analysis.

The statistical analysis of pitch and yaw responses is presented in Figure 4.11 and Figure 4.12. As can be observed the mean pitch and yaw values remain consistently low across all sea states, which shows desirable platform stability. However, it's worth mentioning that the standard deviation of pitch increases with the severity of the sea state. This suggests a greater change in pitch response under more extreme conditions. In contrast to surge response, the maximum pitch response is observed at DLC16. This was expected due to the increased aerodynamic forces on the blades at rated wind speed which consequently leads to increased pitch motion. Although, the difference in maximum pitch values between DLC16 and DLC61 is negligible.

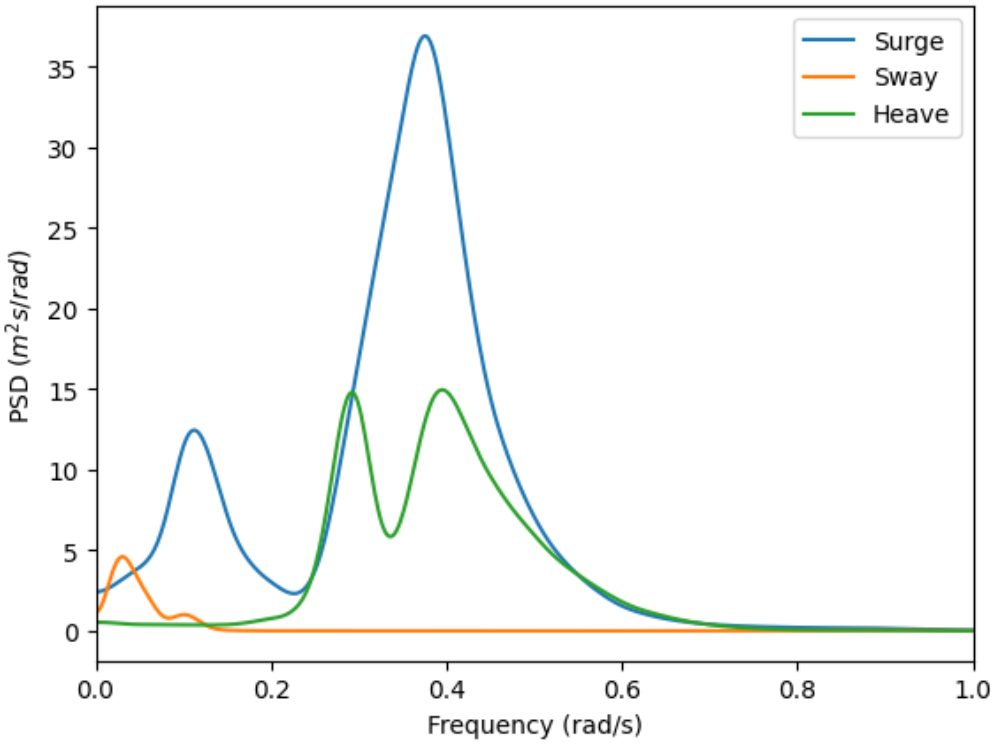

Figure 4.8 PSD of the platform in transitional DOFs.

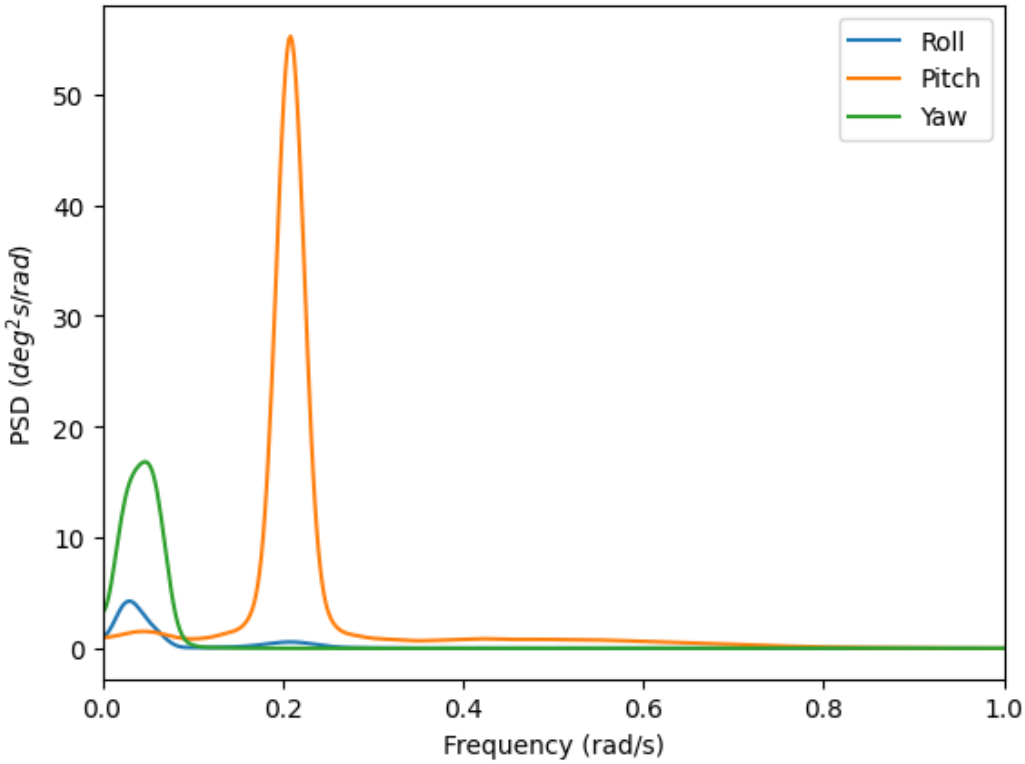

Figure 4.9 PSD of the platform in rotational DOFs.

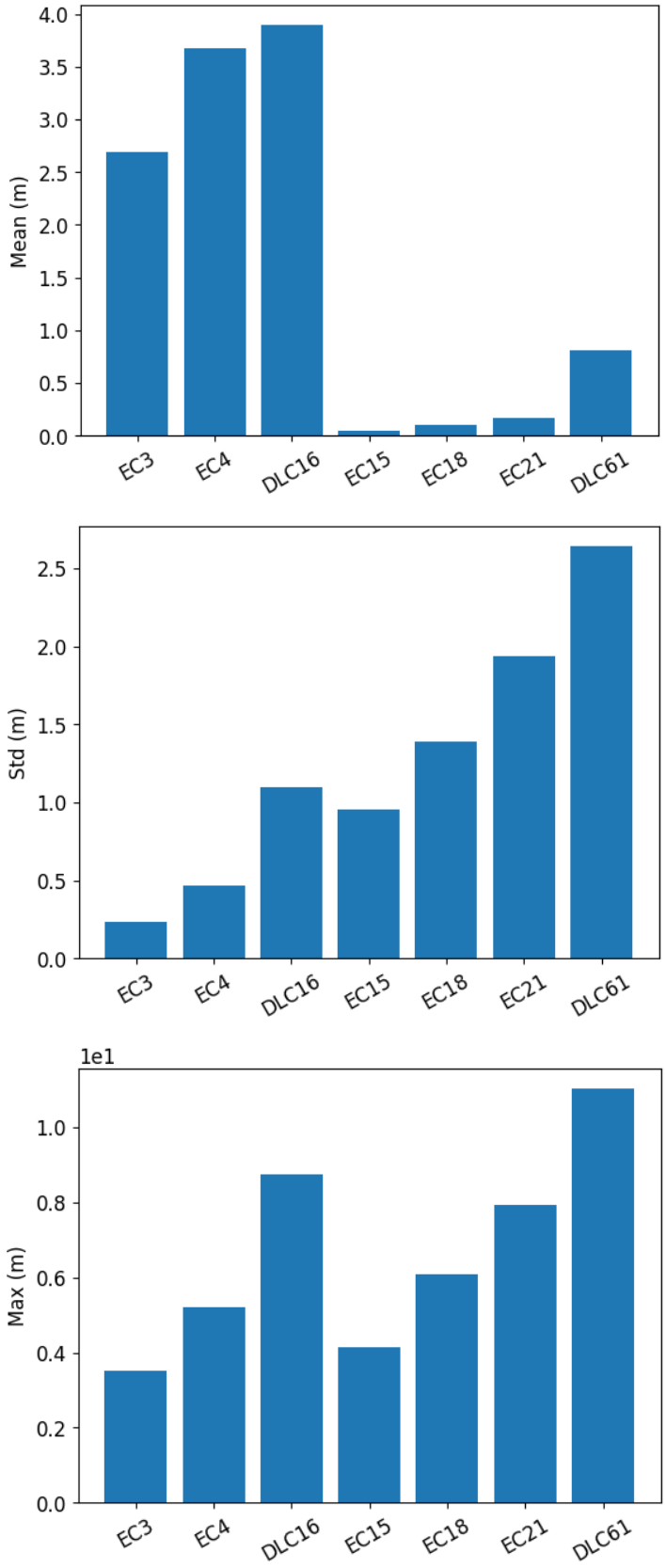

Figure 4.10 Surge Motion Response.

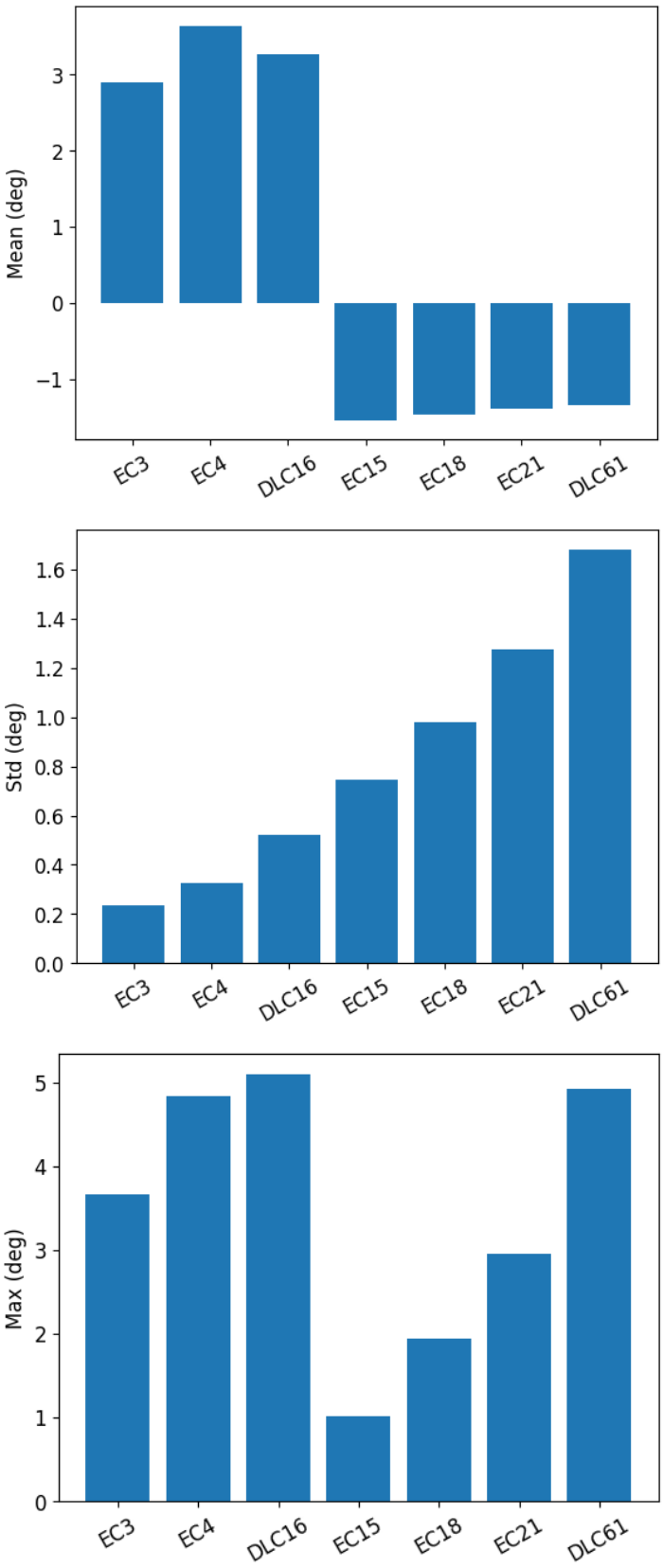

Figure 4.11 Pitch Motion Response.

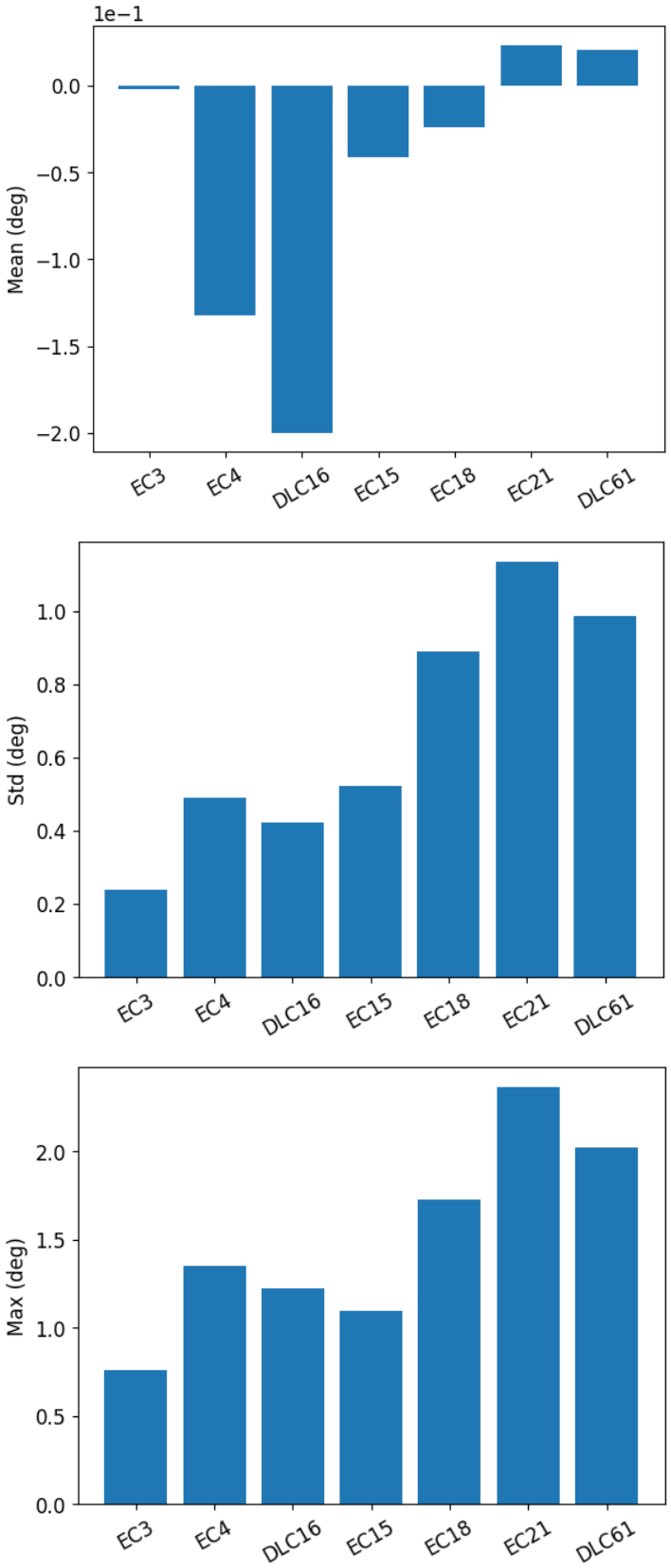

Figure 4.12 Yaw Motion Response.

4.5 Mooring line tension

Figure 4.13 shows the windward mooring line tension for a selected number of sea states including the two design load cases DLC16 and DLC61. As expected, the mean mooring line tension at the rated wind speed extreme condition DLC16 is the maximum due to the maximum surge displacement of the platform.

Immediately after the DLC16 a significant decrease in mooring line tension is observed which is in line with the surge displacement as was observed in Figure 4.10. Although the highest mean tension occurs at DLC16, the maximum tension and the largest standard deviation for this tension occur at DLC61. As a result, DLC61 is more critical for extreme load case analysis and should be paid more attention to during the design of the platform and mooring system.

4.6 Extreme response analysis

As demonstrated previously in Figure 3.6, the extreme tension response of the windward mooring line is higher in DLC61 compared to DLC16. This was anticipated based on the results shown in Figure 4.10 as the larger maximum surge displacement of the platform in DLC61 corresponds to a larger tension in the windward mooring line. This signifies the importance of DLC61 in the extreme load case analysis again similar to what was discussed in the previous part.

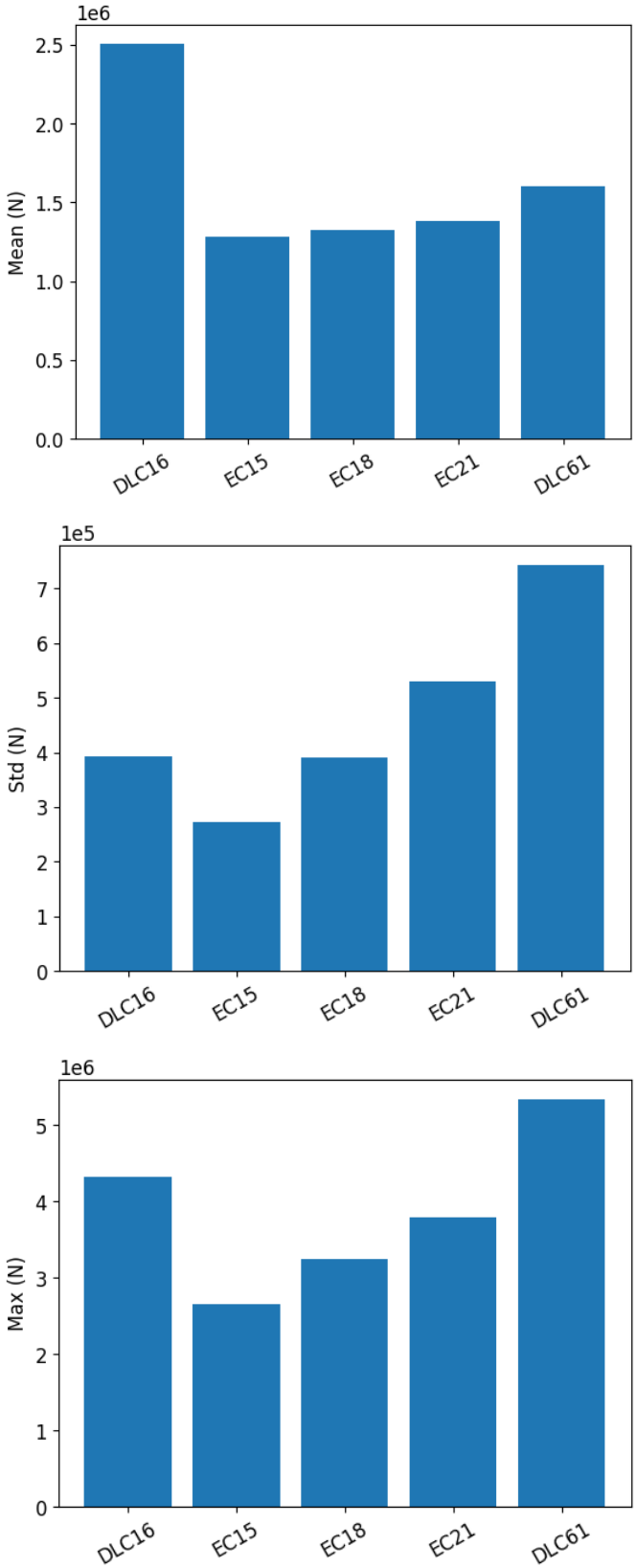

Figure 4.13 Windward mooring line tension statistics.

4.7 Fatigue environmental bin selection

The results of the MDA bin selection are presented in Table 4.4. By setting the distance tolerance to 0.15, 20 sea state clusters were generated for the fatigue analysis. This resulted in a bin quality of 94.5% while limiting the number of simulations to a manageable amount. Table 4.5 also shows the different MDA outputs with different distance tolerances and the number of generated clusters with their respective quality.

Table 4.4 Environmental bins selected by MDA algorithm. The green color represents wind speeds below rated speed, yellow represents above rated, and red represents above the cutout speed.

#	H_S (m)	T_P (s)	U_W (m/s)	TI	Probability
1	1.127	7.457	4.462	3.838	8.78%
2	1.284	11.474	5.342	3.94	1.54%
3	0.962	4.898	5.765	3.988	13.86%
4	1.487	7.389	8.657	4.313	12.95%
5	1.539	9.976	9.119	4.365	5.21%
6	0.771	3.178	9.719	4.431	0.65%
7	1.376	5.586	10.680	4.536	12.33%
8	2.918	9.038	10.740	4.543	3.84%
9	2.055	13.178	11.726	4.65	1.14%
10	1.955	7.822	12.788	4.765	10.71%
11	2.281	10.201	14.171	4.913	4.52%
12	1.601	5.563	14.565	4.955	5.30%
13	3.889	9.658	15.958	5.102	3.70%
14	2.517	7.506	16.490	5.158	6.84%
15	3.450	11.882	17.658	5.28	1.53%
16	2.009	9.954	18.121	5.328	0.73%
17	3.578	8.799	19.857	5.508	3.19%
18	5.127	10.564	21.472	5.673	2.14%
19	5.442	12.763	22.026	5.73	0.44%
20	7.240	12.273	26.056	6.135	0.59%

Table 4.5 Clusters created (M) with respect to distance tolerance (d_{tol}) and quality of bins (q).

d_{tol}	M	q (%)
0.00	1E+06	100.00
0.05	264	97.40
0.08	96	96.30
0.15	20	94.50
0.45	4	89.97
1.00	1	0.00

4.8 Mooring line tension statistics

Figure 4.14 shows the windward mooring line tension statistics for the environmental bins presented in Table 4.4. As expected, the tension is highest around the turbine's rated speed similar to what was observed in the response analysis of the platform. As the controller begins pitching the blades after the rated speed, the aerodynamic drag force gradually decreases, resulting in lower thrust force and hence lower surge offset and tension on the mooring line. However, the standard deviation of the load increases gradually with the wind speed, with a small decrease occurring just after the rated wind speed.

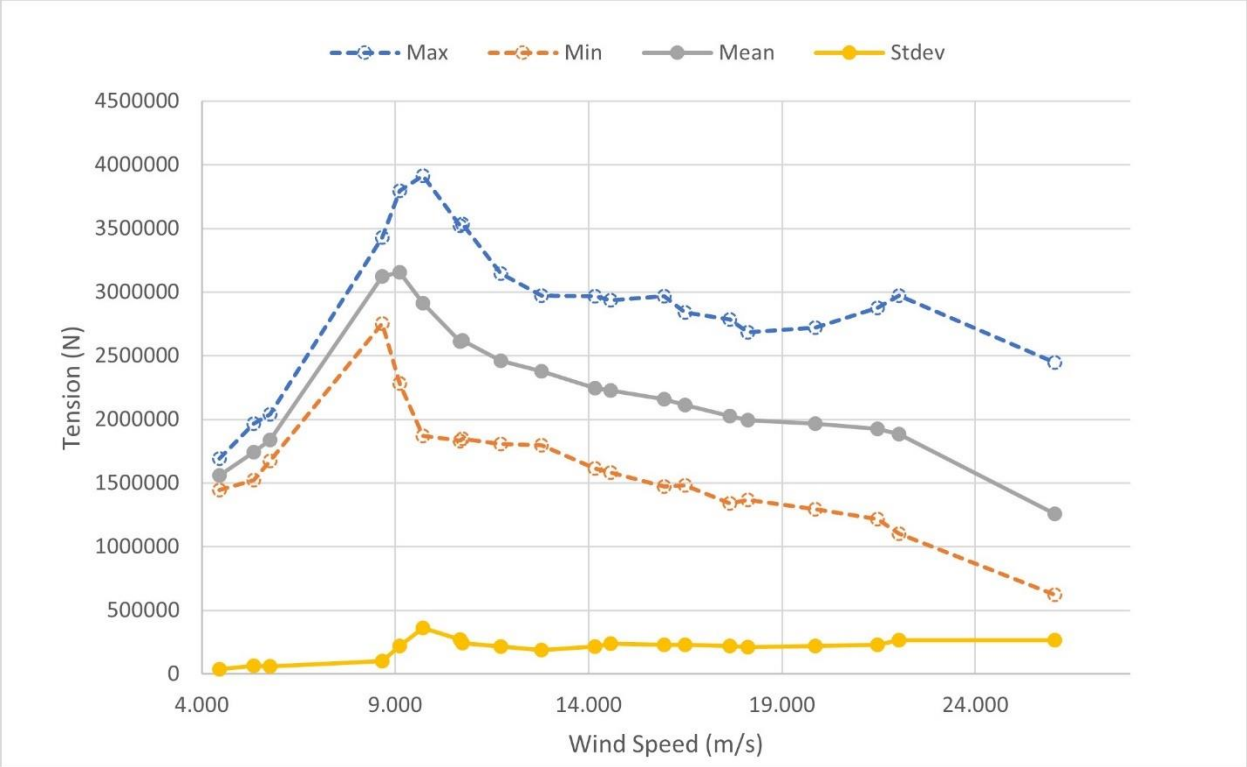

Figure 4.14 Mooring line tension for fatigue environmental bins.

4.9 Fatigue damage

Table 4.6 presents the results of the fatigue damage on the polyester mooring line for six different seeds for each sea state listed in Table 4.4. The fatigue damage was calculated using the TN curve parameters provided in Table 3.7. The yearly fatigue damage (YFD) is determined by multiplying the sea state probability by the average annual damage for each sea state (D_1 to D_6). As shown in the results, the total fatigue summation indicates that the expected life of the polyester line is approximately 1 million years with a safety factor of 1.

As recommended by the American Petroleum Institute (API), it is advisable to use the chain or fairlead segments of the mooring line for fatigue analysis in taut mooring systems, as the TN curve parameters for polyester ropes may not be highly reliable. Consequently, the fatigue analysis

for the chain segment of the mooring at the fairlead was conducted, and the results are presented in Table 4.7. The estimated life of the chain segment at the fairlead is approximately 280 years.

Figure 4.15 compares the fatigue damage for both the polyester and chain segments of the mooring line. Assuming the damage calculation for the polyester segment is accurate, the figure illustrates that the fatigue damage on the chain segment is significantly more pronounced. This finding aligns with the API recommendations, indicating that the chain segment should be a primary concern in the design of the mooring system [57].

It is also worth noting that the fatigue damage in both segments is greatest around the rated wind speed and after the cut-out wind speed. This behavior was expected; the fatigue damage around the rated wind speed is primarily due to aerodynamic forces exerted on the turbine blades, which cause maximum tension on the mooring lines at this point. Conversely, after the cut-out wind speed, the fatigue damage is mainly due to higher wave heights and the heave motion of the platform. These results are in line with the mooring line statistics presented in Figure 4.14.

Table 4.6 Polyester line fatigue damage results from different environmental conditions.

#	D_1	D_2	D_3	D_4	D_5	D_6	$\bar{D}$	YFD
1	7.92E-10	4.21E-11	1.01E-10	2.78E-11	5.95E-11	2.80E-11	1.75E-10	1.54E-12
2	9.54E-09	9.99E-09	6.37E-09	2.15E-08	7.49E-09	6.17E-08	1.94E-08	3.00E-11
3	4.17E-09	4.76E-09	8.85E-09	6.73E-09	1.92E-08	2.05E-08	1.07E-08	1.48E-10
4	1.79E-08	6.81E-09	4.03E-09	4.21E-08	2.00E-09	8.56E-08	2.64E-08	3.42E-10
5	2.63E-07	3.78E-06	5.79E-06	1.66E-06	2.97E-07	6.14E-06	2.99E-06	1.56E-08
6	1.86E-04	1.12E-05	3.76E-04	7.37E-05	1.29E-04	7.79E-05	1.42E-04	9.26E-08
7	8.37E-05	2.97E-06	2.97E-06	6.22E-06	4.87E-05	9.20E-06	2.56E-05	3.16E-07
8	2.01E-06	8.13E-07	7.94E-07	3.18E-07	6.13E-06	1.80E-06	1.98E-06	7.60E-09
9	3.30E-06	4.91E-06	1.11E-06	9.09E-07	5.61E-07	2.06E-06	2.14E-06	2.45E-09
10	4.41E-06	9.75E-07	1.79E-07	1.44E-07	5.01E-06	1.21E-06	1.99E-06	2.13E-08
11	3.15E-06	2.32E-07	3.60E-06	1.56E-07	2.38E-06	1.43E-06	1.82E-06	8.23E-09
12	3.05E-05	2.13E-06	5.46E-06	1.93E-05	1.30E-06	6.33E-06	1.08E-05	5.75E-08
13	1.33E-06	1.12E-06	5.49E-06	2.50E-06	2.58E-06	9.71E-06	3.79E-06	1.40E-08
14	6.89E-06	8.01E-07	1.02E-06	4.96E-07	1.15E-06	1.05E-06	1.90E-06	1.30E-08
15	9.09E-06	1.36E-05	2.68E-06	1.51E-06	3.96E-06	1.08E-05	6.94E-06	1.06E-08
16	2.32E-06	1.74E-07	2.25E-07	3.49E-07	1.25E-06	3.70E-06	1.34E-06	9.73E-10
17	6.34E-07	2.27E-06	5.01E-06	4.78E-07	4.78E-07	4.85E-07	1.56E-06	4.97E-09
18	3.85E-05	1.03E-05	3.86E-05	4.00E-06	7.65E-05	4.87E-05	3.61E-05	7.73E-08
19	2.33E-04	2.11E-05	1.56E-04	1.84E-05	1.45E-04	2.28E-04	1.34E-04	5.86E-08
20	3.05E-04	7.20E-04	1.89E-04	2.52E-04	6.05E-04	2.26E-04	3.83E-04	2.25E-07
Sum	-	-	-	-	-	-	-	9.27E-07

Table 4.7 Mooring chain fatigue damage results from different environmental conditions.

#	D_1	D_2	D_3	D_4	D_5	D_6	$\overline{D}$	YFD
1	2.58E-05	5.14E-06	9.23E-06	4.83E-06	6.01E-06	3.50E-06	9.09E-06	7.98E-07
2	1.90E-04	1.96E-04	1.44E-04	2.33E-04	1.52E-04	5.41E-04	2.43E-04	3.75E-06
3	5.31E-05	1.26E-05	8.07E-05	5.96E-05	1.10E-04	1.00E-04	6.94E-05	9.61E-06
4	1.23E-04	5.93E-05	1.12E-05	4.32E-04	3.08E-05	2.79E-04	1.56E-04	2.02E-05
5	5.15E-04	2.20E-03	3.29E-03	1.11E-03	1.60E-04	2.82E-03	1.68E-03	8.77E-05
6	3.20E-02	6.25E-03	4.91E-02	1.55E-02	2.54E-02	1.91E-02	2.46E-02	1.60E-04
7	1.41E-02	2.83E-03	1.02E-02	4.67E-03	1.28E-02	5.23E-03	8.32E-03	1.03E-03
8	2.53E-03	4.09E-04	1.23E-03	5.66E-04	3.57E-03	1.93E-03	1.71E-03	6.55E-05
9	2.92E-03	5.50E-03	2.32E-03	1.77E-03	1.46E-03	3.15E-03	2.85E-03	3.26E-05
10	3.09E-03	1.21E-03	4.64E-04	1.16E-04	3.00E-03	1.39E-03	1.54E-03	1.65E-04
11	3.36E-03	5.15E-04	3.66E-03	4.88E-04	2.53E-03	1.89E-03	2.07E-03	9.36E-05
12	1.17E-02	5.43E-03	3.80E-03	8.19E-03	1.79E-03	6.63E-03	6.26E-03	3.32E-04
13	2.46E-03	2.05E-03	5.78E-03	2.66E-03	3.12E-03	8.69E-03	4.12E-03	1.53E-04
14	4.44E-03	1.12E-03	1.67E-03	8.62E-04	1.35E-03	1.45E-03	1.82E-03	1.24E-04
15	8.82E-03	1.15E-02	4.56E-03	3.08E-03	4.88E-03	1.01E-02	7.16E-03	1.10E-04
16	2.57E-03	4.72E-04	5.83E-04	8.47E-04	1.69E-03	3.15E-03	1.55E-03	1.13E-05
17	1.45E-03	2.39E-03	4.00E-03	9.37E-04	3.22E-03	1.11E-03	2.18E-03	6.97E-05
18	2.25E-02	9.32E-03	2.24E-02	1.79E-03	2.79E-02	2.78E-02	1.86E-02	3.99E-04
19	6.51E-02	1.73E-02	5.72E-02	1.11E-03	4.81E-02	6.37E-02	4.21E-02	1.85E-04
20	7.83E-02	1.28E-01	5.80E-02	6.89E-02	1.06E-01	6.41E-02	8.39E-02	4.94E-04
Sum	-	-	-	-	-	-	-	3.54E-03

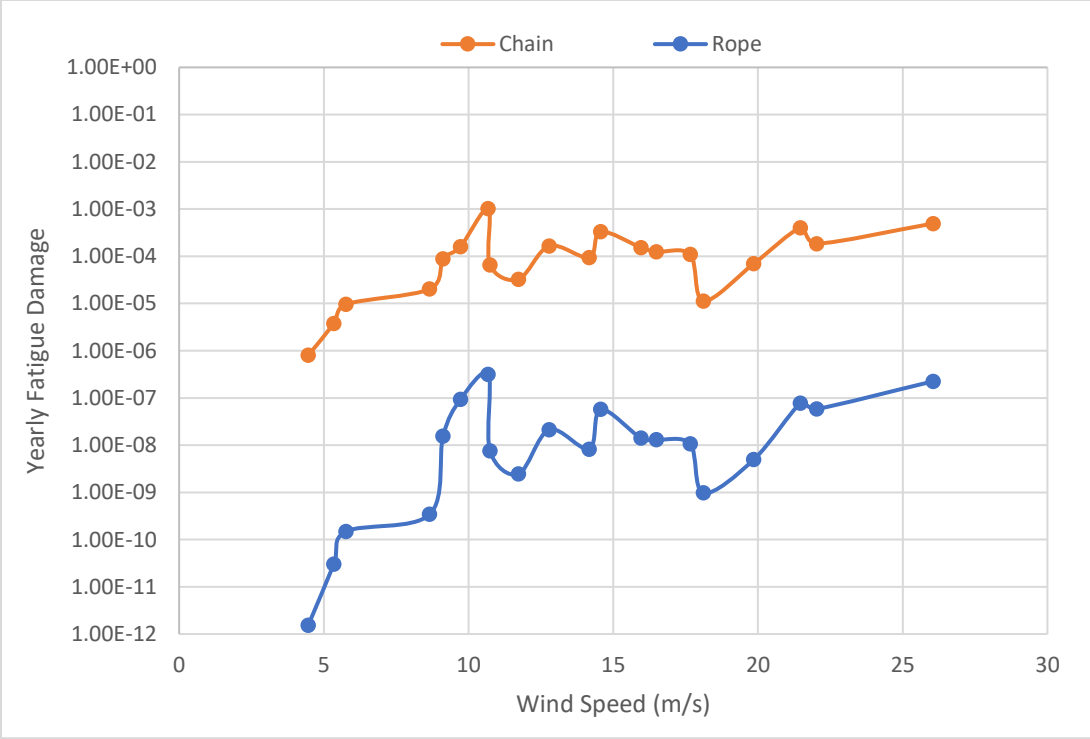

Figure 4.15 Comparison of yearly fatigue damage for the different segments of the mooring line.

5 Conclusions

In this study, we investigated the extreme response analysis of a VolturnUS-S FOWT for the SN II site. Initially, we proposed 5 different mooring system configurations with different lengths of polyester and chain lengths while keeping the anchor radius and pretension the same in all designs. We evaluated the watch circle and the mooring line tensions for each of these designs to select the most suitable for the longevity and also stability of the platform. The results suggested that although the larger bottom chain results in a smaller watch circle and a more stable platform in surge and sway the mooring system with the larger polyester segment reduces the maximum tension on the windward mooring line and hence the MS1 was selected for further investigation such as extreme response analysis and fatigue analysis. It is recommended that in future studies one considers the allowed surge displacement limit and further optimizes this design.

The model was then subjected to different sea states with wind speeds ranging from 4 to 43 m/s and also the two design load cases DLC16 and DLC61. The maximum tension in all cases was fitted into a Gumbel distribution to find the extreme 50-year tension in the mooring line. The results showed the peak of the extreme tension happening at DLC16 but DLC61 after cutout speed showed the larger tension which was mainly due to wave dominant loads exerted on the platform. this showed the significance of DLC61 in the design of the platform and mooring configuration which should be the main focus in extreme load case analysis.

We implemented and used the MDA method to select 20 sea states that are representative of one million sea states. The original sea states are generated according to the joint distribution of sea states for the SN II site. With this approach, the number of required sea states for fatigue analysis was reduced while trying to keep the quality of the analysis high. It is recommended that

a study on the actual effectiveness of the quality metric on the fatigue analysis be performed in future studies.

The results of the fatigue analysis suggest that the polyester rope segment can withstand cyclic loading for a very long period and the focus of fatigue analysis should be on the mooring chain at the fairlead as was recommended by API. This resulted in the investigation of the fatigue damage on the fairlead which showed a fatigue life of approximately 280 years with a safety factor of 1 which shows a reasonable life for the mooring chain. When looking at the fatigue damage for each environmental bin individually it is observed that the fatigue damage becomes large at the rated wind and afterward due to the significant increase in the standard deviation of loads at these sea states. This is synonymous with a higher tension range in each cycle of loading and hence more fatigue damage. It is expected that by decreasing the polyester rope length the estimated fatigue life of the chain at the fairlead would decrease but it is recommended to investigate this in future studies.

In summary, we tried to investigate a mooring system design for the floating offshore wind turbine implementation at the SN II site to increase the mooring system life expectancy while maintaining the stability of the platform. It is also recommended that other synthetic mooring systems be investigated such as nylon for the mooring system and compared to this study.

References

1. Galparsoro, I., et al., *Reviewing the ecological impacts of offshore wind farms.* npj Ocean Sustainability, 2022. **1**(1): p. 1.
2. Dean, N., *Performance factors.* Nature Energy, 2020. **5**(1): p. 5-5.
3. Equinor. *Floating wind*. 2024 [cited 2024 26 Jan]; Available from: https://www.equinor.com/energy/floating-wind.
4. Barooni, M., et al. *Floating offshore wind turbines: Current status and future prospects*. Energies, 2023. **16**, DOI: 10.3390/en16010002.
5. WindEurope. *Wind energy in Europe: 2022 Statistics and the outlook for 2023-2027*. 2023 [cited 2024 23 Jan]; Available from: https://windeurope.org/intelligence-platform/product/wind-energy-in-europe-2022-statistics-and-the-outlook-for-2023-2027/.
6. Gibbs, D. and P.D. Jensen, *Chasing after the wind? Green economy strategies, path creation and transitions in the offshore wind industry.* Regional Studies, 2022. **56**(10): p. 1671-1682.
7. Aldersey-Williams, J., I. Broadbent, and P. Strachan, *Better estimates of LCOE from audited accounts - A new methodology with examples from United Kingdom offshore wind and CCGT.* Energy Policy, 2019. **128**: p. 25-35.
8. Xu, H., et al., *Shared mooring systems for offshore floating wind farms: A review.* Energy Reviews, 2024. **3**(1): p. 100063.
9. Astariz, S. and G. Iglesias, *The economics of wave energy: A review.* Renewable and Sustainable Energy Reviews, 2015. **45**: p. 397-408.

10. Zhou, Y., et al. *Initial design of a novel barge-type floating offshore wind turbine in shallow water*. Journal of Marine Science and Engineering, 2023. **11**, DOI: 10.3390/jmse11030464.

11. Li, G., T. Oh, and G. Zheng, *On the deep-water and shallow-water limits of the intermediate long wave equation from a statistical viewpoint*. 2022.

12. Riyanto, R.D., J.M. Papadopoulos, and A.T. Myers, *Numerical investigation of wave following mechanism of shallow draft floating wind turbine*. 2022.

13. Fjermedal, S., *Mooring design for a combined wind and wave energy system in intermediate water depth*, in *Marine and Offshore Technology*. 2023, University of Stavanger: Stavanger, Norway.

14. Stenlund, T., *Mooring system design for a large floating wind turbine in shallow water*, in *Marine Technology*. 2018, Norwegian University of Science and Technology: Trondheim, Norway.

15. Yang, R., et al., *Current status and future trends for mooring systems of floating offshore wind turbines.* Sustainable Marine Structures, 2022. **4**.

16. Xu, K., et al., *Design and comparative analysis of alternative mooring systems for floating wind turbines in shallow water with emphasis on ultimate limit state design.* Ocean Engineering, 2021. **219**: p. 108377.

17. Buljan, A. *Norway has room for 338 GW of offshore wind, new analysis finds*. 2023 [cited June 2024 8/6]; Available from: https://www.offshorewind.biz/2023/04/21/norway-has-room-for-338-gw-of-offshore-wind-new-analysis-finds/.

18. Cutler, J., et al., *Preliminary development of a novel catamaran floating offshore wind turbine platform and assessment of dynamic behaviours for intermediate water depth application.* Ocean Engineering, 2022. **258**: p. 111769.

19. Power, P. *WindFloat*. 2021 [cited 2024 31/1]; Available from: https://www.principlepower.com/projects/windfloat1.

20. Equinor. *Hywind scotland*. 2022 [cited 2024 31/1]; Available from: https://www.equinor.com/energy/hywind-scotland.

21. Zhang, L., et al., *Second-order hydrodynamic effects on the response of three semisubmersible floating offshore wind turbines.* Ocean Engineering, 2020. **207**: p. 107371.

22. Van Kessel, J.L.F., *Aircushion supported mega floaters.* 2010.

23. Pham, T.D. and H. Shin *A new conceptual design and dynamic analysis of a spar-type offshore wind turbine combined with a moonpool*. Energies, 2019. **12**, DOI: 10.3390/en12193737.

24. Chen, M., et al. *Dynamic analysis of a barge type floating wind turbine subjected to failure of the mooring system*. Journal of Marine Science and Engineering, 2024. **12**, DOI: 10.3390/jmse12040617.

25. Ideol, B. *BW Ideol's first floater in operation*. [cited 2024 31/1]; Available from: https://www.bw-ideol.com/en/floatgen-demonstrator.

26. Adam, F., et al. *Gicon® TLP for wind turbines the path of development*. in *The 1st international conference on renewable energies offshore (RENEW)*. 2014.

27. Guo, T., et al. *Study on tension leg platform's motion response by wave load of 2nd-order difference frequency based on intelligent computation*. in *2022 International Conference on Manufacturing, Industrial Automation and Electronics (ICMIAE)*. 2022.

28. Atcheson, M., et al., *Floating offshore wind energy.* by Joao Cruz and Mairead Atcheson. Springer International Publishing. Chap. Looking back. doi, 2016. **10**(1007): p. 978-3.

29. Zhang, H., et al., *Novel method for designing and optimising the floating platforms of offshore wind turbines.* Ocean Engineering, 2022. **266**: p. 112781.

30. Faltinsen, O., *Sea loads on ships and offshore structures*. Vol. 1. 1993: Cambridge university press.

31. Muhammad, N., Z. Ullah, and D.-H. Choi, *A numerical procedure accounting for fluid drag Forces and cable extensibility for the static response of mooring cables.* International Journal of Steel Structures, 2018. **18**(1): p. 293-303.

32. Zheng, X., et al. *Study on characteristics and optimal layout of components in shallow water mooring system of floating wind turbine*. Applied Sciences, 2022. **12**, DOI: 10.3390/app121910137.

33. Lozon, E., et al., *Design and analysis of a floating-wind shallow-water mooring system featuring polymer springs*. 2022.

34. Sintef. *Load models*. [cited 2024 10/6]; Available from: https://www.sima.sintef.no/doc/4.4.0/riflex/theory/load_models.html#AeroElements.

35. Rodrigues, J.M. *A procedure to calculate first-order wave-structure interaction loads in wave farms and other multi-body structures subjected to inhomogeneous waves*. Energies, 2021. **14**, DOI: 10.3390/en14061761.

36. Rahman, M. and S. Mousavizadegan, *The second-order wave loads on offshore structures using Weber transform.* Far East Journal of Applied Mathematics, 2005. **21**.

37. Orcina. *Second-order equations*. [cited 2024 11/6]; Available from: https://www.orcina.com/webhelp/OrcaWave/Content/html/Theory,Second-orderequations.htm.

38. Jahani, K., F. Afagh, and R. Langlois, *Structural dynamics and vibrations in offshore horizontal axis wind turbines: A review of the state of the art*. 2023.

39. Allen, C., et al., *Definition of the UMaine VolturnUS-S Reference Platform Developed for the IEA Wind 15 Megawatt Offshore Reference Wind Turbine*. 2020, National Renewable Energy Laboratory.

40. BEKARET, B., *Advanced rope solutions for offshore oil and gas exploration*, in *construction and production industries*, B. BEKARET, Editor. 2013.

41. Ramnäs, *Top quality mooring products for harsh offshore conditions*, in *Ramnäs bruk product cataloge*, R.O. AB, Editor. 2012.

42. Sintef. *SIMA*. [cited 2024 25/4]; Available from: https://www.sintef.no/en/software/sima/.

43. DNV. *Frequency domain hydrodynamicanalysis of stationary vessels - WADAM*. [cited 2024 26/4]; Available from: https://www.dnv.com/services/frequency-domain-hydrodynamic-analysis-of-stationary-vessels-wadam-2412/.

44. Falkenberg, E., V. Åhjem, and L. Yang, *Best practice for analysis of polyester rope mooring systems*, in *Offshore Technology Conference*. 2017.

45. DNV, *Design, testing and analysis of offshore fibre ropes*. 2021.

46. Ćatipović, I., et al. *Numerical modelling for synthetic fibre mooring lines taking elongation and contraction into account*. Journal of Marine Science and Engineering, 2021. **9**, DOI: 10.3390/jmse9040417.

47. Xiong, L., et al., *Numerical simulation of nonlinearity and viscoelasticity of synthetic fibre rope for taut moorings in deep water.* Ships and Offshore Structures, 2018. **13**(2): p. 132-142.

48. Sørum, S.H., et al. *Modelling of synthetic fibre rope mooring for floating offshore wind turbines*. Journal of Marine Science and Engineering, 2023. **11**, DOI: 10.3390/jmse11010193.

49. Cheynet, E., L. Li, and Z. Jiang, *Metocean conditions at two Norwegian sites for development of offshore wind farms.* Renewable Energy, 2024. **224**: p. 120184.

50. Al-Solihat, M. and M. Nahon, *Mooring and hydrostatic restoring of offshore floating wind turbine platforms*. 2015.

51. Montasir, O.A., A. Yenduri, and V.J. Kurian, *Effect of mooring line properties and fairlead slopes on the restoring behavior of offshore mooring system.* Research Journal of Applied Sciences, Engineering and Technology, 2014. **8**: p. 346-353.

52. Ja'E, I., M. Ahmed, and A. Yenduri, *Numerical studies on the effects of mooring configuration and line diameter on the restoring behaviour of a turret-moored FPSO*. 2020.

53. Shipping, A.B.o., *Guide for building and classing floating offshore wind turbines*, in *Design Load Conditions*. 2024.

54. Haselsteiner, A., J.-H. Ohlendorf, and K.-D. Thoben, *Environmental contours based on kernel density estimation*. 2017.

55. Li, Q., Z. Gao, and T. Moan, *Modified environmental contour method to determine the long-term extreme responses of a semi-submersible wind turbine.* Ocean Engineering, 2017. **142**: p. 563-576.

56. Ekberg, A., *Fatigue of railway wheels*, in *Wheel–Rail Interface Handbook*, R. Lewis and U. Olofsson, Editors. 2009, Woodhead Publishing. p. 211-244.

57. Ma, K.-T., et al., *Fatigue analysis*, in *Mooring System Engineering for Offshore Structures*, K.-T. Ma, et al., Editors. 2019, Gulf Professional Publishing. p. 115-137.

58. Lee, Y.-L., M.E. Barkey, and H.-T. Kang, *Metal fatigue analysis handbook: practical problem-solving techniques for computer-aided engineering*. 2012, Butterworth-Heinemann: Waltham, Mass.

59. Halfpenny, A., *A frequency domain approach for fatigue life estimation from finite element analysis.* Key Engineering Materials, 1999. **167-168**: p. 401-410.

60. Huang, G., et al., *One-stage extraction four-point algorithm for rainflow cycle counting in fatigue life estimation.* Engineering Computations, 2023. **40**(1): p. 126-148.

61. Kanner, S., et al., *Maximum dissimilarity based algorithm for discretization of metocean data Into clusters of arbitrary size and dimension*. 2018.

62. Camus, P., et al., *Analysis of clustering and selection algorithms for the study of multivariate wave climate.* Coastal Engineering, 2011. **58**(6): p. 453-462.

Appendix A: Python code for polyester rain flow counting and fatigue damage calculation

```
# reading the data
import matplotlib.pyplot as plt
import openpyxl as xl
import numpy as np


# Input the file name here and transient time
transient_time = 400

wb = xl.load_workbook('SampleName.xlsx')
ws = wb['data']
rows = ws.max_row


sim_time = ws[f'A[61]'].value - transient_time


def get_tension(_index):
    return ws[f'B[4]'].value


def get_time(_index):
    return ws[f'A[4]'].value


tensions = []
for row in range(2, rows+1):
    if get_time(row) >= transient_time:
        tensions.append(get_tension(row))


# Hysteresis filtering
hysteresis_gate = 0

tension_filtered = [tensions[0]]
for index in range(1, len(tensions)):
    if abs(tensions[index] - tensions[index -1]) > hysteresis_gate:
        tension_filtered.append(tensions[index])
    else:
        continue
```

```
# Peak value filtering
peaks = [tension_filtered[0]]

for index in range(1, len(tension_filtered)-1):
    if tension_filtered[index] > tension_filtered[index-1] and
tension_filtered[index] > tension_filtered[index+1]:
        peaks.append(tension_filtered[index])
    elif tension_filtered[index] < tension_filtered[index-1] and
tension_filtered[index] < tension_filtered[index+1]:
        peaks.append(tension_filtered[index])

peaks.append(tension_filtered[-1])

# Binning (bin segments should usually be more than 64)
bin_count = 1024
bin_gate = (max(peaks) - min(peaks)) / (bin_count - 1)

binned_peaks = []
for value in peaks:
    value -= min(peaks)
    a = value%bin_gate
    b = value//bin_gate
    if a < 0.5*bin_gate:
        binned_peaks.append(min(peaks)+(b)*bin_gate)
    else:
        binned_peaks.append(min(peaks)+(b+1)*bin_gate)

# Rain flow counting (Four-point method)
rf_matrix = []
for i in range(bin_count):
    rf_matrix.append([0] * bin_count)


def evaluate_points(points):
    return(abs(binned_peaks[points[0]] - binned_peaks[points[3]]) >=
abs(binned_peaks[points[1]] - binned_peaks[points[2]]))


def make_matrix(_indices):
    if evaluate_points(_indices):
        removed_values = [binned_peaks.pop(_indices[1]),
binned_peaks.pop(_indices[1])]
        row = int((removed_values[0] - min(binned_peaks))/ bin_gate)
        col = int((removed_values[1] - min(binned_peaks))/ bin_gate)
        rf_matrix[row][col] += 1
```

```
    else:
        _indices = [x+1 for x in _indices]
        if _indices[3] < len(binned_peaks):
            make_matrix(_indices)
        else:
            return


while len(binned_peaks) >= 4:
    preLength = len(binned_peaks)
    indices = [0, 1, 2, 3]
    make_matrix(indices)

    if preLength == len(binned_peaks):
        break

# Ploting the residuals
residuals = binned_peaks
cycle_count = len(residuals)
x = np.linspace(1, cycle_count, cycle_count)
plt.plot(x, residuals)
plt.show()

# Plotting the rainflow diagram
x = []
y = []
colors = []
possible_values = list(np.linspace(min(binned_peaks), max(binned_peaks),
bin_count))

for i in range(len(rf_matrix)):
    for j in range(len(rf_matrix[i])):
        if rf_matrix[i][j] > 0 :
            x.append(possible_values[i])
            y.append(possible_values[j])
            colors.append(rf_matrix[i][j])

plt.scatter(x, y, c=colors, edgecolors='gray', alpha=0.6, cmap=plt.cm.rainbow)
plt.xlabel('From (N)')
plt.ylabel('To (N)')
cbar = plt.colorbar()
cbar.set_label(label='cycles count', size = 12)
plt.show()
```

```
# TN curve (tension vs cycles) from API for Polyester rope
k_parameter = 25000
m_parameter = 5.2
MBS = 11772000

# Tension for this function should be given in N
def get_failureCycles(tension_range):
    R = tension_range/MBS
    return k_parameter/pow(R, m_parameter)


sim_damage = 0
for i in range(len(rf_matrix)):
    for j in range(len(rf_matrix[i])):
        stress_range = abs(possible_values[i]-possible_values[j])
        if stress_range != 0:
            sim_damage += rf_matrix[i][j] / get_failureCycles(stress_range)

# Defining safety factors and getting damage result
sf = 1
yearly_damage = ((365 * 24 * 3600 * sf) / sim_time) * sim_damage
print('hourly damage:', yearly_damage/(365*24))
print('yearly fatigue damage:', yearly_damage)
print('estimated life (in years):' , 1/yearly_damage)
```

Appendix B: Python code for MDA

```
import openpyxl as xl
from matplotlib import pyplot as plt
import itertools

wb = xl.load_workbook('DataName.xlsx')
ws = wb.active
rows = ws.max_row
original_points = []

for row in range(2, rows+1):
    original_points.append([ws[f'A[4]'].value, ws[f'B[4]'].value,
ws[f'C[4]'].value])

data_count = len(original_points)

x, y, z = [], [], []
for i in range(len(original_points)):
    x.append(original_points[i][0])
    y.append(original_points[i][1])
    z.append(original_points[i][2])

dimentions = len(original_points[0])

# Normalization
x_max = max(x)
y_max = max(y)
z_max = max(z)

for point in original_points:
    point[0] /= x_max
    point[1] /= y_max
    point[2] /= z_max

x, y, z = [], [], []
for i in range(len(original_points)):
    x.append(original_points[i][0])
    y.append(original_points[i][1])
    z.append(original_points[i][2])

points = original_points.copy()

# define tolerance distance and initiate clusters dictionary
```

```
d_tolerance = 0.15
clusters = [4]
clusters_centeroid = [4]

# All functions
# points distances
def distance(pointA, pointB):
    result = 0
    for i in range(dimentions):
        result += pow(pointB[i] - pointA[i] ,2)
    return pow(result ,0.5)


# Average of n-dimensional data points
def dimentional_average(_cluster):
    avgs = [0] * dimentions
    for _point in _cluster:
        for i in range(dimentions):
            avgs[i] += _point[i]

    for i in range(dimentions):
        avgs[i] /= len(_cluster)

    return avgs


# finds the centroid of a cluster
def update_cluster_pos():
    for cluster in clusters:
        if len(clusters[cluster]) == 0:
            return
        clusters_centeroid[cluster] = dimentional_average(clusters[cluster])


# clear clusters for redistribution
def clear_clusters():
    for cluster in clusters:
        clusters[cluster] = []


# adds new members to cluster by distance from the centroid
removed_points = []
def populate_clusters():

    update_cluster_pos()
    clear_clusters()
```

```
    print(len(points)- len(removed_points), 'points remaining')
    for i in range(len(points)):
        if i !=0 and i % 200000 == 0:
            print(100 * i / len(points), '%...')
        for j in range(len(clusters_centeroid)):
            if points[i] != 'x' and distance(points[i], clusters_centeroid[j+1])
< d_tolerance:
                removed_points.append(points[i])
                points[i] = 'x'

    for point in removed_points:
        min_distance = distance([0]*dimentions, [1]*dimentions)
        chosen_cluster = 1
        for i in range(len(clusters)):
            if distance(point, clusters_centeroid[i+1]) <= min_distance:
                min_distance = distance(point, clusters_centeroid[i+1])
                chosen_cluster = i+1

        clusters[chosen_cluster].append(point)

    update_cluster_pos()


# Find candidates for max distance (a fast method that does not go through all
points)
def find_initial_candidates(_points):
    candidate_initials = []
    for i in range(dimentions):
        min_basket = []
        isFilled_min = False
        max_basket = []
        isFilled_max = False
        delta_distance = 0.01
        while not isFilled_min or not isFilled_max :
            for point in _points:
                if not isFilled_min and point[i] <= delta_distance and point not
in min_basket and point not in candidate_initials:
                    min_basket.append(point)
                if not isFilled_max and point[i] >= 1 - delta_distance and point
not in max_basket and point not in candidate_initials:
                    max_basket.append(point)
            delta_distance += delta_distance
            if delta_distance > 1:
                break
            if len(min_basket) != 0: isFilled_min = True
```

```
            if len(max_basket) != 0: isFilled_max = True

        candidate_initials += (min_basket + max_basket)
    print('initial candidate length:' ,len(candidate_initials))
    return candidate_initials


# find the max distance between points (a large number of points makes this super
slow so use find initial candidates first)
def max_distance_finder(_pointslist):
    max_dis = 0
    pointA = [0] * dimentions
    pointB = [0] * dimentions
    for i in range(len(_pointslist)):
        for j in range(len(_pointslist)):
            if i != j and distance(_pointslist[i], _pointslist[j]) > max_dis:
                max_dis = distance(_pointslist[i], _pointslist[j])
                pointA = _pointslist[i]
                pointB = _pointslist[j]

    return [pointA, pointB]


# Cluster finder
def find_clusters():
    if len(clusters) == 0:
        print('finding initail points ...')
        candidates = find_initial_candidates(points)
        initials = max_distance_finder(candidates)
        p1 = initials[0]
        p2 = initials[1]
        print('initial clusters found!')
        removed_points.append(p1)
        removed_points.append(p2)
        clusters[1] = [p1]
        clusters[2] = [p2]
        p1, p2 = 'x', 'x'
        print('initail points found!')
        populate_clusters()
    else:
        min_distances = []
        for i in range(len(points)):
            if points[i] == 'x':
                min_distances.append(0)
                continue
```

```
            min_distance = distance([0]*dimentions, [1]*dimentions)
            for centeroid in clusters_centeroid:
                if distance(points[i], clusters_centeroid[centeroid]) <=
min_distance:
                    min_distance = distance(points[i],
clusters_centeroid[centeroid])
            min_distances.append(min_distance)

        pt = points[min_distances.index(max(min_distances))]
        if pt == 'x':
            print(min_distances.index(max(min_distances)))
            print(min_distances)
        removed_points.append(pt)
        clusters[len(clusters)+1] = [pt]
        pt = 'x'
        print('cluster', len(clusters) ,'found')
        print('populating cluster...')
        populate_clusters()

# Initiation (finding the first two clusters)
find_clusters()

plt.scatter(x,y,z, c ='gray')


marker = itertools.cycle((',', '+', '.', 'o', '*', 'v', '^', '1', '3'))
for i in range(len(clusters)):
    clusterX = []
    clusterY = []
    clusterZ = []
    for point in clusters[i+1]:
        clusterX.append(point[0])
        clusterY.append(point[1])
        clusterZ.append(point[2])

    plt.scatter(clusterX, clusterY, marker = next(marker))

update_cluster_pos()

# cluster creation loop
while (len(removed_points) < len(points)):
    find_clusters()

update_cluster_pos()
```

```
plt.scatter(x, y, z, c = 'gray')
for i in range(len(clusters)):
    clusterX = []
    clusterY = []
    for point in clusters[i+1]:
        clusterX.append(point[0])
        clusterY.append(point[1])

    plt.scatter(clusterX, clusterY, marker=next(marker))

avg_x = []
avg_y = []
for i in range(len(clusters_centeroid)):
    avg_x.append(clusters_centeroid[i+1][0])
    avg_y.append(clusters_centeroid[i+1][1])

    plt.scatter(avg_x, avg_y, marker='*', c='black')

# A 2D representation of the clusters formed
plt.title('All Clusters')
plt.show()
print('Total Clusters:', len(clusters))

# Probability distribution of each cluster
pdf = []
for cluster in clusters:
    probability = len(clusters[cluster]) / data_count
    pdf.append(probability)
    clusters_centeroid[cluster].append(probability)

# Cumulative distribution of each cluster for sanity check to see if it reaches 1
cdf = [pdf[0]]
for i in range(1, len(pdf)):
        cdf.append(cdf[i-1] + pdf[i])

x_cdf = np.linspace(0, len(cdf), len(cdf))
plt.plot(x_cdf, cdf)
plt.show()

# Finding the quality of MDA
q_res = 0
for i in range(len(clusters)):
    clus_dist = 0
    for j in range(len(clusters[i+1])):
        clus_dist += distance(clusters[i+1][j], clusters_centeroid[i+1])
```

```
    clus_dist *= 1/len(clusters[i+1])
    q_res += clus_dist

quality = 100 * (1 - q_res/len(clusters))
print('q =', quality)

# Creating and saving the results file
if 'res' not in wb:
    ws = wb.create_sheet('res')
else:
    ws = wb['res']

max_values = [x_max, y_max, z_max, 1]

for i in range(len(clusters_centeroid)):
    for j in range(len(clusters_centeroid[i+1])):
        ws.cell(row=i+1, column=j+1).value = clusters_centeroid[i+1][j] *
max_values[j]

wb.save('results.xlsx')

# 3D visualization of the results
%matplotlib widget
fig = plt.figure()
ax = fig.add_subplot(projection='3d')

for i in range(len(clusters)):
    x, y, z = [], [], []

    for j in range(len(clusters[i+1])):
        x.append(clusters[i+1][j][0])
        y.append(clusters[i+1][j][1])
        z.append(clusters[i+1][j][2])

    ax.scatter(x, y, z, alpha=0.05)


ax.set_xlabel('Hs')
ax.set_ylabel('Tp')
ax.set_zlabel('Uw')
plt.show()
```